RESEARCH ARTICLE SUMMARY

INFLAMMASOMES

HDAC6 mediates an aggresome-like mechanism for NLRP3 and pyrin inflammasome activation

Venkat Giri Magupalli*†, Roberto Negro*†, Yuzi Tian*, Arthur V. Hauenstein*, Giuseppe Di Caprio, Wesley Skillern, Qiufang Deng, Pontus Orning, Hasan B. Alam, Zoltan Maliga, Humayun Sharif, Jun Jacob Hu, Charles L. Evavold, Jonathan C. Kagan, Florian I. Schmidt, Katherine A. Fitzgerald, Tom Kirchhausen, Yongqing Li†, Hao Wu†

INTRODUCTION: Canonical inflammasomes are multicomponent protein complexes that play key roles in immune surveillance of infections and danger by activating caspase-1, which cleaves interleukin 1β (IL-1β) and the pore-forming protein gasdermin D, leading to cytokine maturation and pyroptosis. The nucleotide-binding domain, leucine-rich repeat, and pyrin domain–containing protein 3 (NLRP3) can be activated by the bacterial toxin nigericin, extracellular ATP, and various particulates such as monosodium urate (MSU) crystals, alum, silica, and amyloids, whereas the pyrin inflammasome can be stimulated by the Rho-glucosylation activity of *Clostridium difficile* toxin B. One important hallmark for inflammasome activation is the formation of a single supramolecular punctum (also known as a speck) per cell. However, the location and trafficking of such puncta remain unknown.

RATIONALE: To decode the site and the molecular machinery in inflammasome assembly and activation in macrophages, we aimed to visualize inflammasome assembly by cellular imaging complemented by pharmacological inhibition and targeted deletion in cells and in mice.

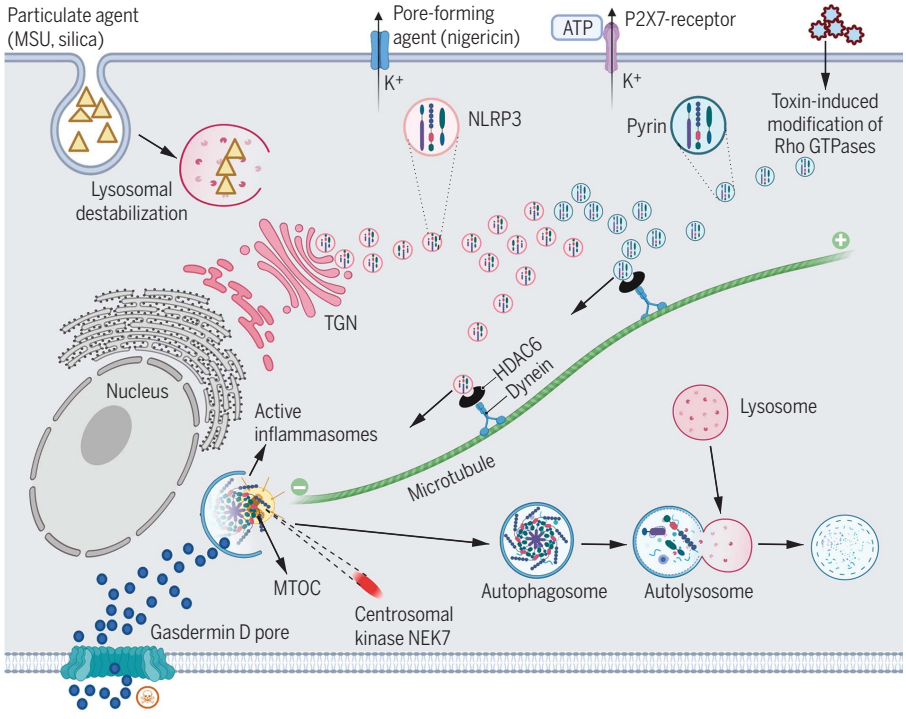

HDAC6- and microtubule-dependent assembly and activation of NLRP3 and pyrin inflammasomes. Multiple stimuli for NLRP3 (MSU, silica, nigericin, and ATP) and pyrin (Rho GTPase modification) are shown on the top part of the cell. NLRP3 and pyrin inflammasome components are represented in pink and light blue, respectively. NLRP3 inflammasome assembly may involve two steps: initial oligomerization at the TGN and further assembly into a single punctum with the centrosomal kinase NEK7, the adaptor ASC, and caspase-1 at the MTOC. The latter is achieved after being retrograde transported on the microtubule by the HDAC6-dynein machinery. Pyrin inflammasome activation also requires HDAC6, dynein, and microtubules. Assembled inflammasomes at the MTOC are subject to degradation by autophagy in a manner similar to aggresomes that degrade pathological aggregates. [Figure was created with BioRender (https://BioRender.com).]

RESULTS: We found that NLRP3 and pyrin inflammasomes are assembled at the centrosome, also known as the microtubule-organizing center (MTOC), of each cell, which serves as the major site for caspase-1 activation and IL-1β conversion. Pharmacological inhibitors of microtubule polymerization, dynein ATPase and the dynein adaptor histone deacetylase 6 (HDAC6), and targeted deletion or knockdown of *Hdac6* compromised the assembly and activation of these inflammasomes. Reconstitution of *Hdac6*$^{-/-}$ macrophages showed that the ubiquitin-binding ability of HDAC6, but not its deacetylase activity, is required for NLRP3 and pyrin inflammasome activation. In mice, *Hdac6* deficiency reduced lipopolysaccharide- and MSU-induced inflammation to a similar extent as direct NLRP3 inhibition, which demonstrates the requirement of HDAC6 and the microtubule retrograde transport machinery for NLRP3 activation. By contrast, AIM2 and NLRC4 inflammasome puncta do not localize at the MTOC, and these inflammasomes do not require microtubule retrograde transport for their activation. Thus, our studies revealed a specific mechanism of inflammasome activation for NLRP3 and pyrin.

For the NLRP3 inflammasome, MTOC localization may facilitate association with the centrosome-localized kinase NEK7 to enhance inflammasome assembly. We found that in *Hdac6*$^{-/-}$ macrophages, NLRP3 is trapped as small speckles at the trans-Golgi network (TGN), a previously recognized common site for NLRP3 association upon induction by multiple NLRP3 stimulators. These data suggested that HDAC6-mediated microtubule transport delivers NLRP3 from TGN to the MTOC. The NLRP3 inflammasome formed at the MTOC colocalizes with LC3b, an autophagy marker, and an autophagy inhibitor enhances NLRP3-induced IL-1β secretion.

CONCLUSION: Our study reveals an unexpected parallel between HDAC6-dependent assembly of NLRP3 and pyrin inflammasomes and the formation of aggresomes at the MTOC for autophagic degradation of ubiquitinated pathological aggregates. The dual activating and inhibiting roles played by the MTOC localization of NLRP3 and pyrin inflammasomes may be critical for achieving balanced inflammasome regulation. ■

The list of author affiliations is available in the full article online.
*These authors contributed equally to this work.
†Corresponding author: Email: wu@crystal.harvard.edu (H.W.); venkat.magupalli@childrens.harvard.edu (V.G.M.); roberto.negro@childrens.harvard.edu (R.N.); yqli@med.umich.edu (Y.L.)
Cite this article as V. G. Magupalli *et al.*, *Science* **369**, eaas8995 (2020). DOI: 10.1126/science.aas8995

READ THE FULL ARTICLE AT
https://doi.org/10.1126/science.aas8995

Downloaded from http://science.sciencemag.org/ on September 18, 2020

RESEARCH ARTICLE

INFLAMMASOMES

HDAC6 mediates an aggresome-like mechanism for NLRP3 and pyrin inflammasome activation

Venkat Giri Magupalli[1,2]*†, Roberto Negro[1,2]*†, Yuzi Tian[3,4]*, Arthur V. Hauenstein[1,2]*, Giuseppe Di Caprio[2,5], Wesley Skillern[2], Qiufang Deng[3,4], Pontus Orning[6,7], Hasan B. Alam[3], Zoltan Maliga[8], Humayun Sharif[1,2], Jun Jacob Hu[1,2], Charles L. Evavold[9], Jonathan C. Kagan[9], Florian I. Schmidt[10], Katherine A. Fitzgerald[6,7], Tom Kirchhausen[2,5], Yongqing Li[3]†, Hao Wu[1,2]†

Inflammasomes are supramolecular complexes that play key roles in immune surveillance. This is accomplished by the activation of inflammatory caspases, which leads to the proteolytic maturation of interleukin 1β (IL-1β) and pyroptosis. Here, we show that nucleotide-binding domain, leucine-rich repeat, and pyrin domain–containing protein 3 (NLRP3)- and pyrin-mediated inflammasome assembly, caspase activation, and IL-1β conversion occur at the microtubule-organizing center (MTOC). Furthermore, the dynein adapter histone deacetylase 6 (HDAC6) is indispensable for the microtubule transport and assembly of these inflammasomes both in vitro and in mice. Because HDAC6 can transport ubiquitinated pathological aggregates to the MTOC for aggresome formation and autophagosomal degradation, its role in NLRP3 and pyrin inflammasome activation also provides an inherent mechanism for the down-regulation of these inflammasomes by autophagy. This work suggests an unexpected parallel between the formation of physiological and pathological aggregates.

Inflammasomes play important roles in cytosolic host defense (*1*–*5*). Architecturally, canonical inflammasomes are composed of an upstream sensor, an adapter, and the downstream caspase-1 (*6*). By contrast, in noncanonical inflammasomes, when bacterial lipopolysaccharide (LPS) gains access to the cytosol, it directly engages and activates caspase-4 and -5 in humans and caspase-11 in mice (*1*). Nucleotide-binding domain, leucine-rich repeat, and pyrin domain–containing protein 3 (NLRP3) constitutes an extensively studied inflammasome sensor, which can be activated by diverse stimuli including the bacterial pore-forming toxin nigericin, extracellular ATP, and various particulates such as monosodium urate (MSU) crystals, alum, and silica (*2*–*4*). Activated NLRP3 recruits the apoptosis-associated speck-like protein containing a CARD (ASC), which in turn recruits caspase-1 (Fig. 1A). Absent in melanoma 2 (AIM2) and pyrin are sensors for two other ASC-dependent inflammasomes. AIM2 is activated by cytosolic double-stranded DNA (dsDNA), and pyrin can be stimulated by Rho-glucosylation activity of *Clostridium difficile* toxin B (TcdB) (*2*, *7*) (Fig. 1A). The NLR family CARD-containing protein 4 (NLRC4) can form an inflammasome with or without ASC upon complex formation with an NLR family apoptosis inhibitory protein (NAIP), which directly senses bacterial flagellin or type III secretion system proteins (*1*–*5*). The formation of inflammasomes leads to proximity-induced caspase dimerization, activation, and autoprocessing. Caspase-1 cleaves pro–interleukin 1β (pro–IL-1β) and pro–IL-18 to generate the mature cytokines, and caspase-1, -4, -5, and -11 can proteolytically activate gasdermin D to form membrane pores for cytokine release and pyroptosis (*2*–*4*, *8*–*10*). Dysregulated inflammasome activity has been implicated in numerous human diseases, including hereditary autoinflammatory syndromes and common conditions such as gout, diabetes, atherosclerosis, Alzheimer's disease, and colorectal cancer (*2*–*5*).

NLRP3 and pyrin inflammasomes, but not the AIM2 inflammasome, localize at the MTOC

An intriguing observation has been that many inflammasomes assemble into a single major perinuclear punctum in each activated cell (*11*, *12*). The singularity and perinuclear nature of an inflammasome punctum led us to investigate its connection, if any, with the centrosome, which also acts as the microtubule-organizing center (MTOC) in eukaryotic cells and is perinuclear and punctate in appearance. We used both the human monocytic cell line THP-1 and immortalized mouse bone marrow–derived macrophages (iBMDMs), which endogenously express NLRP3 and other inflammasome components. NLRP3 and ASC colocalized with the centrosomal markers ninein and γ-tubulin (GTU) (*13*) upon priming by LPS and activation by MSU or nigericin (Fig. 1, B and C, and fig. S1, A to C). When THP-1 cells were stimulated with MSU, 88.5% (62/70 cells) showed colocalization between ASC and ninein. By contrast, only 1.4% (1/70 cells) lacked apparent colocalization. The location of the remaining ASC puncta could not be determined because of the lack of corresponding ninein staining. Similarly, 80% (40/50) of MSU-stimulated THP-1 cells exhibited ASC colocalization with GTU, 4% (2/50 cells) showed no colocalization, and the remaining 16% (8/50) showed no visible GTU staining. NEK7, a member of the NIMA-related kinase (NEK) family, which predominantly resides at the MTOC and is required for NLRP3 inflammasome activation (*14*–*16*), also colocalized with ASC and GTU (fig. S1D). The specificity of anti-NLRP3 and anti-ASC antibodies was thoroughly validated (figs. S1, E and F, and S2). Thirty minutes after nigericin stimulation, robust caspase-1 processing (fig. S3, A and B) and IL-1β secretion (fig. S3C) were observed.

In addition to NLRP3 and ASC, IL-1β also localized at the inflammasome puncta (fig. S3, D and E). Labeling of active caspase-1 by FAM-FLICA (*17*) showed that in 9% (2/22) and 18% (4/22) of cells, respectively, active caspase-1 completely and partially colocalized with the ASC puncta (fig. S3F, examples 1 and 2). In most cells (73%, 16/22), active caspase-1 surrounded the ASC punctum (fig. S3F, example 3), suggesting that caspase-1 is first activated at an inflammasome punctum by dimerization and then released into the cytosol upon autocleavage from the N-terminal CARD prodomain. Thus, NLRP3 inflammasome puncta at the MTOC may serve as a major site for both caspase-1 activation and IL-1β conversion.

We attempted to visualize NLRP3 inflammasome activation using live-cell imaging of fluorescent protein–fused ASC. However, unlike wild-type (WT) cells, nigericin stimulation induced an iBMDM cell line stably expressing ASC-mRuby3 and a THP-1 cell line expressing ASC-TagRFP-T to form puncta distinctly away from the MTOC marked by SiR-tubulin, a live-cell fluorogenic probe for microtubules (fig. S4, A to C, and movie S1). By contrast, an iBMDM cell line stably expressing Flag-ASC showed that the main puncta formed upon nigericin stimulation, which were visualized by anti-Flag

[1]Department of Biological Chemistry and Molecular Pharmacology, Harvard Medical School, Boston, MA 02115, USA. [2]Program in Cellular and Molecular Medicine, Boston Children's Hospital, Boston, MA 02115, USA. [3]Department of Surgery, North Campus Research Complex, University of Michigan, Ann Arbor, MI 48109, USA. [4]Department of Rheumatology and Immunology, Xiangya Hospital, Central South University, Changsha, Hunan, China. [5]Departments of Cell Biology and Pediatrics, Harvard Medical School, Boston, MA 02115, USA. [6]Program in Innate Immunity, Department of Medicine, Division of Infectious Diseases and Immunology, University of Massachusetts Medical School, Worcester, MA 01605, USA. [7]Centre of Molecular Inflammation Research, Department of Clinical and Molecular Medicine, Norwegian University of Science and Technology, 7491 Trondheim, Norway. [8]Laboratory of Systems Pharmacology, Harvard Medical School, Boston, MA 02115, USA. [9]Harvard Medical School and Division of Gastroenterology, Boston Children's Hospital, Boston, MA 02115, USA. [10]Institute of Innate Immunity, Biomedical Center, University Hospitals, University of Bonn, Venusberg-Campus 1, 53127 Bonn, Germany.
*These authors contributed equally to this work.
†Corresponding author. Email: wu@crystal.harvard.edu (H.W.); venkat.magupalli@childrens.harvard.edu (V.G.M.); roberto.negro@childrens.harvard.edu (R.N.); yqli@med.umich.edu (Y.L.)

Downloaded from http://science.sciencemag.org/ on September 18, 2020

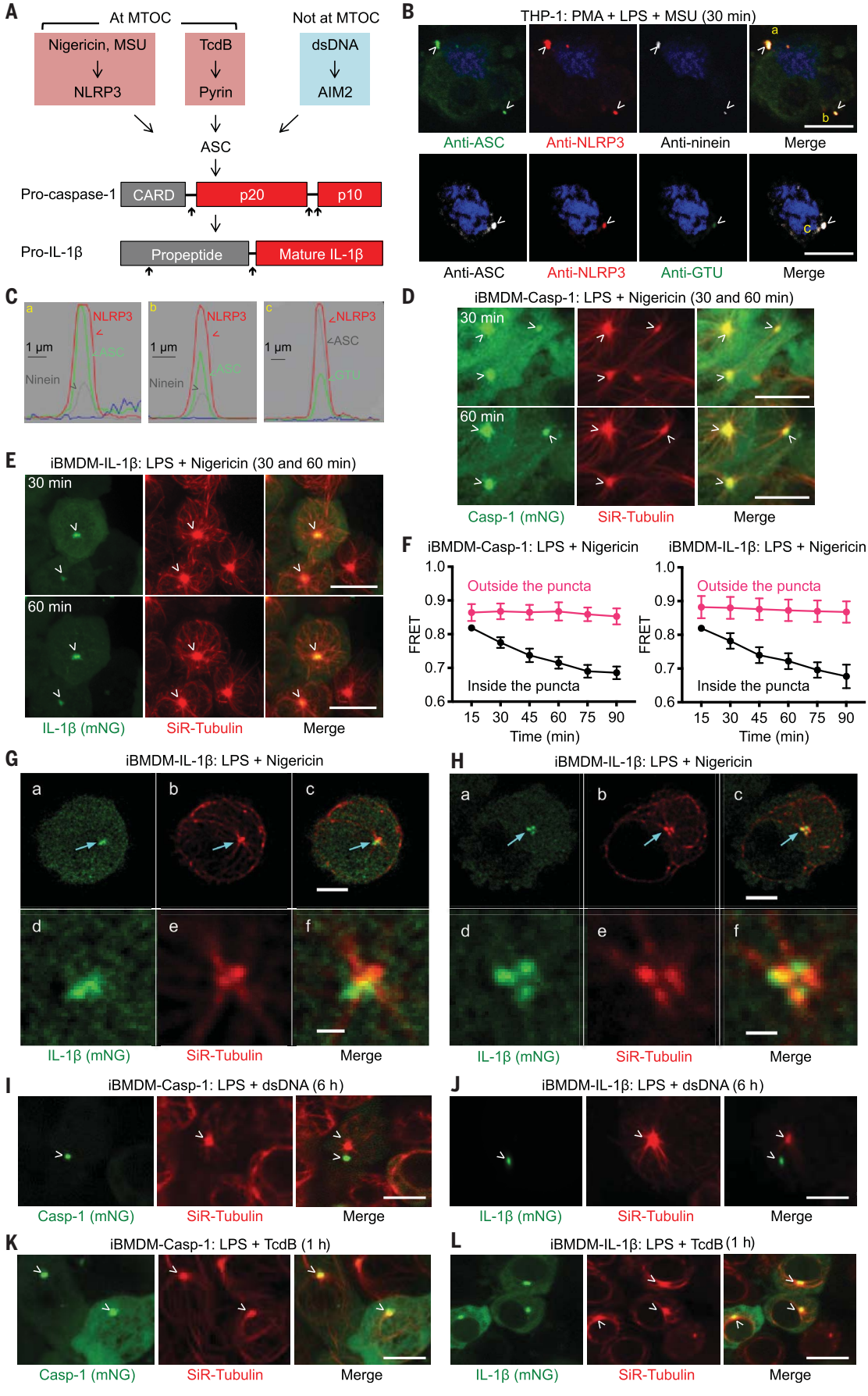

Downloaded from http://science.sciencemag.org/ on September 18, 2020

Fig. 1. NLRP3 and pyrin inflammasomes, but not the AIM2 inflammasome, colocalize with the MTOC. (**A**) The NLRP3, pyrin, and AIM2 inflammasome pathways triggered by nigericin or MSU, TcdB, and dsDNA, respectively. As shown below, NLRP3 and pyrin inflammasome puncta localize at the MTOC. Inflammasome activation culminates in pro–caspase-1 and pro–IL-1β processing. Upward arrows indicate processing sites. (**B**) Immunofluorescence images showing the colocalization of NLRP3 and ASC puncta with the centrosomal markers ninein and GTU in THP-1 cells. Blue represents nuclear staining by Hoechst 33342. (**C**) Line scan of intensity distribution profiles of puncta a, b, and c from (B). (**D** and **E**) Live-cell images of iBMDM–Casp-1 (D) and iBMDM–IL-1β (E) at 30 min (top panel) and 60 min (bottom panel) after nigericin stimulation showing colocalization of inflammasome puncta (depicted by mNeonGreen) with the MTOC (depicted by SiR-Tubulin staining that labels the microtubule network). (**F**) FRET analysis of caspase-1 cleavage and IL-1β processing at MTOC as a function of time for areas inside and outside the puncta in iBMDM–Casp-1 (left) and iBMDM–IL-1β (right) cells. FRET was calculated by dividing the FRET channel fluorescence intensity (donor excitation with acceptor emission) with mTurquoise2 channel fluorescence intensity (donor excitation with donor emission). Data are shown as mean ± SD for n = 10 to 15 cells. (**G** and **H**) Recruitment of IL-1β to a region in proximity to the MTOC imaged using 3D LLSM. iBMDM–IL-1β cells stained with SiR-Tubulin were exposed to nigericin for 12 min (G) and 23 min (H). (**a** to **c**) Representative images deconvolved using the Richardson–Lucy algorithm corresponding to a single optical plane section. The arrows highlight the MTOC and the nearby locations where IL-Iβ was recruited. (**d** to **f**) Enlarged images of the regions indicated by the arrows. (**I** and **J**) Lack of colocalization of AIM2 inflammasome puncta with the MTOC in iBMDM–Casp-1 (I) and iBMDM–IL-1β (J) cells activated by dsDNA for 6 hours. (**K** and **L**) Colocalization of pyrin inflammasome puncta with the MTOC in iBMDM–Casp-1 (K) and iBMDM–IL-1β (L) cells activated by TcdB toxin for 1 hour. Images are representative of three or more independent experiments, and arrowheads indicate puncta or MTOC [(B), (D), (E), and (G) to (L)]. Scale bars: 10 μm [(B), (D), (E)], 5 μm [(G), (a) to (c); (H), (a) to (c); and (I) to (L)], and 1 μm [(G), (d) to (f), and (H), (d) to (f)].

immunofluorescence, coincided with the MTOC (fig. S4D), suggesting that the green fluorescent protein (GFP) family of tags may have led to nonphysiological localization of ASC. Consequently, we did not use ASC for live-cell imaging of inflammasomes. Instead, we used iBMDM stable cell lines expressing fluorescent protein–fused pro–caspase-1 (iBMDM–Casp-1) or pro–IL-1β (iBMDM–IL-1β).

To track both location and cleavage, a fluorescence resonance energy transfer (FRET) pair, mTurquoise2 (mTur) at the N terminus and mNeonGreen (mNG) at the C terminus, was fused together (fig. S5A). Both pro–caspase-1 and pro–IL-1β formed puncta at the MTOC upon nigericin stimulation (Fig. 1, D and E; fig. S5, B and C; and movies S2 and S3). For some cells, we also observed signal trails from the inflammasome puncta that matched the microtubule staining pattern (Fig. 1D, 60 min), suggesting trafficking of inflammasome complexes on the microtubule network. Three-dimensional (3D) lattice light-sheet microscopy (LLSM) (*18*) of nigericin-stimulated iBMDM-IL-1β cells at 12 and 23 min after treatment, respectively, further revealed that IL-1β was recruited to a region in close proximity to but not overlapping with the MTOC (Fig. 1, G and H, and movie S4). For both iBMDM–IL-1β and iBMDM–Casp-1 cells, FRET signals inside the puncta were high at the beginning, consistent with tethered FRET pairs, but decreased significantly with time, consistent with proteolytic processing (Fig. 1F). By contrast, the FRET signals outside the puncta stayed high (Fig. 1F). Thus, it is upon recruitment to the MTOC that pro–caspase-1 and pro–IL-1β are processed and activated.

To activate the AIM2 inflammasome, iBMDM–Casp-1 and iBMDM–IL-1β cells were transfected with dsDNA. Unlike NLRP3 stimulation, the puncta induced by AIM2 activation did not colocalize with the MTOC despite the dependence on ASC that was similar to that of NLRP3 (Fig. 1, I and J). By contrast, when iBMDM–Casp-1 and iBMDM–IL-1β cells were stimulated with TcdB to activate the pyrin inflammasome, activation-induced puncta colocalized with the MTOC (Fig. 1, K and L, and movies S5 and S6). Similarly, immunofluorescent staining with anti-pyrin, anti-ASC, and anti-ninein antibodies confirmed the MTOC localization of the pyrin inflammasome (fig. S6).

Microtubule retrograde transport by HDAC6 is important for NLRP3 and pyrin inflammasome activation

A major cellular mechanism for the clearance of ubiquitinated protein aggregates, which are too large to be effectively degraded by the ubiquitin proteasome pathway, requires retrograde transport by the dynein adapter and the α-tubulin deacetylase HDAC6 to form aggresomes at the MTOC for degradation by autophagy (*19*–*23*). The aggresome pathway is thought to play an important role in the regulation of protein aggregation diseases such as Alzheimer's disease and age-related macular degeneration (*19*, *21*). Viruses including the influenza A virus are known to subvert the host aggresome pathway by forming viral inclusions at the MTOC in an HDAC6-dependent manner to facilitate replication and assembly (*24*, *25*). The MTOC localization of NLRP3 and pyrin inflammasome puncta, their aggresome-like meshwork morphology (*26*), and ubiquitination of NLRP3 inflammasome components (*27*–*30*) suggest a possible link between inflammasomes and aggresomes.

To test the effects of HDAC6 and microtubule retrograde transport inhibition on NLRP3 function, we pretreated LPS-primed iBMDM–Casp-1 and iBMDM–IL-1β cells with microtubule, dynein, and HDAC6 inhibitors (*31*–*33*). Nigericin stimulation in iBMDM–Casp-1 and iBMDM–IL-1β cells pretreated with these inhibitors invariably failed to induce the generation of puncta. By contrast, untreated nigericin-stimulated cells readily formed puncta (fig. S7, A and B). Inhibitor pretreatment of WT iBMDMs markedly decreased nigericin-induced caspase-1 processing (Fig. 2A), propidium iodide (PI) permeability (Fig. 2B), and IL-1β release (Fig. 2C and fig. S7C) without affecting nuclear factor κB–dependent priming as measured by tumor necrosis factor α (TNFα) secretion (fig. S8A). Dynamitin (also known as p50) is a subunit of the dynactin complex important in dynein function, the overexpression of which disrupts dynein-dependent transport (*34*). Stable expression of mRuby3-fused dynamitin in iBMDM–Casp-1 and iBMDM–IL-1β cells severely compromised nigericin-induced punctum formation without affecting the MTOC localization of NEK7 (figs. S7, A and B, and S8B and movie S7) and caused defective caspase-1 processing, PI permeability, and IL-1β secretion (fig. S8, C to E). Thus, the microtubule-dynein machinery and the HDAC6 adapter both appear to be essential for NLRP3 inflammasome activation.

Our data contradict a previous report that increased α-tubulin acetylation upon NLRP3 stimulation is responsible for dynein-dependent microtubule-mediated assembly of the NLRP3 inflammasome (*35*). Treatment with the HDAC6 inhibitors tubastatin A, rocilinostat, and tubacin markedly increased α-tubulin acetylation. However, instead of increasing NLRP3 inflammasome activation, this treatment inhibited it (Fig. 2, A and D). MCC950, a control NLRP3 inhibitor that interferes with NLRP3 oligomerization (*36*), did not alter α-tubulin acetylation but potently impeded NLRP3 activation (Fig. 2D). Thus, retrograde transport by HDAC6 on the microtubule network aids NLRP3 and pyrin inflammasome activation independently of α-tubulin acetylation.

We investigated the effects of pharmacological inhibition and dynamitin overexpression in other inflammasomes. Consistent with the colocalization of the pyrin inflammasome with the MTOC, treatment with microtubule, dynein, and HDAC6 inhibitors or dynamitin expression hindered TcdB-induced punctum formation (fig. S9, A to D) and compromised TcdB-induced caspase-1 processing, PI permeability, and

Downloaded from http://science.sciencemag.org/ on September 18, 2020

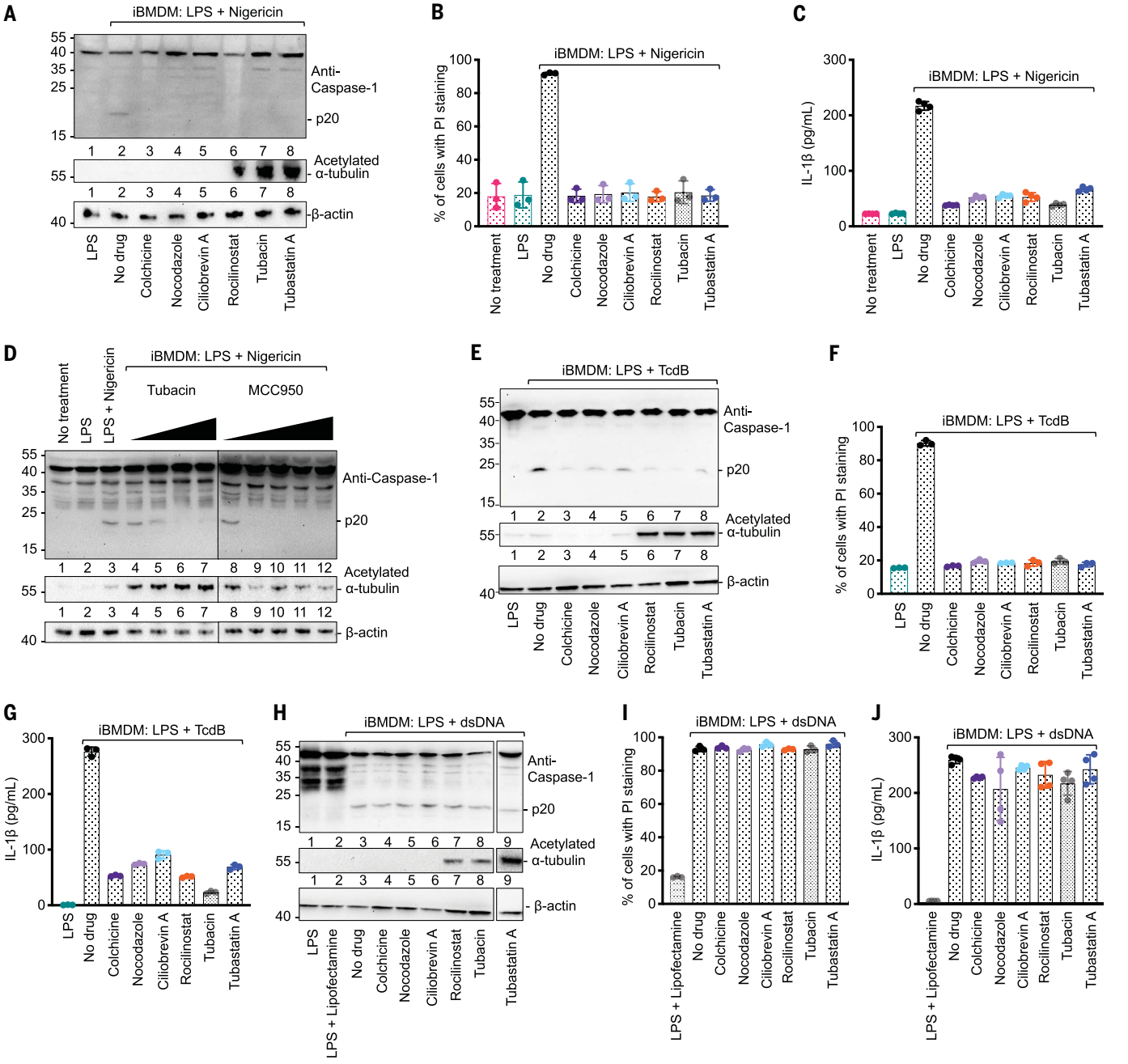

Fig. 2. Microtubule retrograde transport is required for the activation of NLRP3 and pyrin inflammasomes but not the AIM2 inflammasome. (**A** to **C**) NLRP3 inflammasome activation under various inhibition conditions analyzed by caspase-1 processing (p20) (A), quantification of PI permeability by flow cytometry (B), and secreted IL-1β quantified by ELISA (C). Colchicine and nocodazole are microtubule polymerization inhibitors; ciliobrevin A is a dynein ATPase inhibitor; and rocilinostat, tubacin, and tubastatin A are HDAC6 inhibitors. (**D**) Caspase-1 processing (p20) upon NLRP3 inflammasome activation with pretreatment of increasing concentrations of tubacin (left to right: 5, 10, 20, and 40 μM) or the NLRP3 inhibitor MCC950 (left to right: 0.1, 0.5, 1, 10, and 20 μM). Anti–acetylated α-tubulin and anti–β-actin immunoblots are shown for tubulin acetylation and as the loading control, respectively. (**E** to **G**) Pyrin inflammasome activation under various pharmacological conditions analyzed by caspase-1 processing (p20) (E), PI permeability (F), and secreted IL-1β (G). (**H** to **J**) AIM2 inflammasome activation under various pharmacological conditions analyzed by caspase-1 processing (p20) (H), PI permeability (I), and secreted IL-1β (J). Data are shown as the mean ± SD for three or four wells from three or more independent experiments.

IL-1β release (fig. S8, C to E, and Fig. 2, E to G). It is possible that the pyrin inflammasome is even more sensitive to microtubule transport inhibitors than the NLRP3 inflammasome. This is reflected in previous studies in which lower concentrations of colchicine (1 to 4 μM) inhibited the pyrin inflammasome alone (*37*, *38*), whereas higher concentrations of colchicine (5 to 15 μM), as in the present study (10 μM), affected both the pyrin and NLRP3 inflammasome (*35*). In contrast to the NLRP3 and pyrin inflammasomes, neither pharmacological treatment nor dynamitin expression inhibited dsDNA-induced AIM2 inflammasome punctum formation (fig. S10, A

Downloaded from http://science.sciencemag.org/ on September 18, 2020

to D), caspase-1 processing, cell death, or IL-1β secretion (Fig. 2, H to J, and fig. S8, C to E), consistent with its failure to colocalize with the MTOC. Thus, HDAC6 is important for the activation NLRP3 and pyrin inflammasomes but not the AIM2 inflammasome.

HDAC6 targeting compromises NLRP3 inflammasome activation

To further investigate the role of HDAC6 in inflammasome activation, we generated an HDAC6-deficient iBMDM cell line (*Hdac6*$^{-/-}$) using the CRISPR/Cas9 system (*39*). Genomic polymerase chain reaction (PCR) confirmed that the targeting resulted in an internal deletion of the *Hdac6* gene (fig. S11A) and lack of HDAC6 protein expression (Fig. 3A). Normal physiology of *Hdac6*$^{-/-}$ iBMDMs was reflected in the unperturbed centrosome structure (fig. S11B), NEK7 distribution at the centrosome (fig. S11C), and transferrin uptake (fig. S11, D and E). HDAC6 deficiency also did not affect the expression of NLRP3, pyrin, ASC, pro–caspase-1, or pro–IL-1β upon LPS priming (fig. S11, F and G). However, the absence of HDAC6 resulted in markedly reduced caspase-1 cleavage (Fig. 3B), PI permeability (Fig. 3C), IL-1β secretion (Fig. 3D), and punctum formation (movies S8 and S9) upon nigericin stimulation.

To test the possibility that HDAC6 may have a role in ligand accessibility for NLRP3 stimuli that require endocytosis, we used several additional NLRP3 ligands. These included ATP, which directly engages its cell surface P2X7 receptor and should not depend on cellular uptake, as well as silica and alum, which are NLRP3-activating particulates and may require ligand accessibility. HDAC6 deficiency impaired caspase-1 cleavage, PI permeability, and IL-1β secretion after both ATP (fig. S12A) and silica and alum stimulation (fig. S12B). Additionally, puncta were formed upon treatment with all these ligands, whereas few puncta were observed in similarly treated *Hdac6*$^{-/-}$ iBMDMs (fig. S13, A to C). Thus, HDAC6 dependency exists for a broad range of NLRP3 activators regardless of their exact mechanism of action.

To corroborate the *Hdac6*$^{-/-}$ studies, we knocked down the expression of HDAC6 RNA and protein using small interfering RNA (siRNA) and the Trim-Away system (*40*), respectively. Seventy-two hours after iBMDMs were transfected with siRNA, HDAC6 was knocked down (fig. S14A) and iBMDMs exhibited markedly reduced nigericin-stimulated caspase-1 activation (fig. S14A), cell death (fig. S14B), and IL-1β secretion (fig. S14C). Similarly, electroporation of anti-HDAC6 antibody into TRIM21-iBMDMs resulted in substantial HDAC6 degradation after 24 hours (fig. S14D) and reduced caspase-1 processing (fig. S14D), PI permeability (fig. S14E), and IL-1β secretion (fig. S14F) after nigericin stimulation. By contrast, a previous study using small hairpin RNA (shRNA) targeting HDAC6 showed modestly enhanced NLRP3 inflammasome activation in iBMDMs compared with a scrambled shRNA (*41*). However, no untreated iBMDMs were used as a control and it is unclear whether these shRNAs had off-target effects. Thus, these data further support the hypothesis that HDAC6 plays an important role in NLRP3 inflammasome activation.

HDAC6 ubiquitin-binding domain, but not deacetylase activity, is required for NLRP3 activation

We reconstituted *Hdac6*$^{-/-}$ iBMDMs with human WT *HDAC6* and its deacetylase catalytic mutant H216A/H611A (DA) (*42*) (Fig. 3E and fig. S15A). WT *HDAC6* rescued caspase-1 activation upon nigericin stimulation (Fig. 3F). Unexpectedly, the deacetylase activity was not required to support NLRP3 inflammasome activation because the HDAC6 DA also restored NLRP3 inflammasome activation, as shown by caspase-1 processing (Fig. 3G), PI permeability (fig. S15B), and IL-1β secretion (fig. S15C). The effects of small-molecule HDAC6 inhibitors on inflammasome activation may be due to the inability of inhibitor-bound HDAC6 to interact with dynein (*42*, *43*). Indeed, WT *HDAC6*-reconstituted *Hdac6*$^{-/-}$ iBMDMs were sensitive to the HDAC6 inhibitor rocilinostat. By contrast, *HDAC6* DA–reconstituted *Hdac6*$^{-/-}$ iBMDMs were insensitive to rocilinostat (Fig. 3H) because the inhibitor binding requires an intact active site. The α-tubulin deacetylase activity of HDAC6 is also not required for HDAC6- and microtubule-mediated chemotaxis of T lymphocytes (*44*), whereas misfolded protein–induced aggresome formation appeared to require this catalytic activity (*22*). Thus, HDAC6 supports NLRP3 inflammasome activation by its scaffolding role in dynein-mediated transport without the need for its catalytic activity.

The C-terminal region of HDAC6 contains a zinc-finger domain for ubiquitin interaction (*20*). We reconstituted *Hdac6*$^{-/-}$ iBMDMs with the zinc-coordinating mutant H1160/H1164A (Ub1) and ubiquitin-binding site mutant W1182A (Ub2) (Fig. 3E and fig. S15A). Both mutants failed to rescue NLRP3 inflammasome activation shown by caspase-1 processing (Fig. 3G), PI permeability (fig. S15B), and IL-1β secretion (fig. S15C). Live-cell imaging of *Hdac6*$^{-/-}$ iBMDM–Casp-1 cells transiently transfected with mRuby3-fused WT human *HDAC6* showed a correlation between HDAC6 expression and punctum formation. Only cells with detectable HDAC6 expression formed puncta (Fig. 3I and movie S10). Furthermore, *Hdac6*$^{-/-}$ iBMDM–Casp-1 and iBMDM–IL-1β cells stably reconstituted with WT and DA mutant of mRuby3-HDAC6 rescued punctum formation, whereas those transfected with the zinc-finger mutants did not (Fig. 3J, fig. S15D, and movies S11 to S18). Rocilinostat inhibited punctum formation in WT *HDAC6* reconstituted *Hdac6*$^{-/-}$ iBMDM–Casp-1 cells (Fig. 3J). Furthermore, NLRP3 activation by ATP, silica, and alum, as shown by PI permeability (fig. S16) and punctum formation (fig. S17), had the same dependence on the ubiquitin-interacting domain. Thus, HDAC6's ubiquitin-binding function is essential for its role in the NLRP3 inflammasome.

Inflammasome puncta at the MTOC are subjected to autophagic regulation

Because HDAC6-mediated aggresome formation at the MTOC facilitates autophagosomal degradation, we hypothesized that inflammasome puncta are also subject to this regulation. Before nigericin stimulation, there was no colocalization of ASC with the microtubule-associated protein 1 light chain 3b (LC3b), a standard autophagosomal marker (Fig. 3K). By contrast, at 30 min after stimulation, ASC-containing inflammasome puncta were highly enriched in LC3b, suggesting induction of autophagy (Fig. 3L). We previously showed by anti-ASC immunogold electron microscopy (EM) that dense perinuclear structures represent inflammasome puncta (*26*). Here, we observed that the single perinuclear inflammasome punctum was surrounded by double-membrane bilayers, which are suggestive of autophagosome formation (fig. S18). LLSM analysis showed adjacency between an inflammasome punctum and the MTOC per se (Fig. 1, G and H). Thus, inflammasome puncta may be selectively engulfed without affecting the MTOC. Consistent with these findings, reduction or deficiency of the autophagic proteins LC3b, beclin-1, p62, and Atg16L1 can enhance inflammasome activation and maturation of IL-1β and IL-18 (*30*, *45*, *46*). Furthermore, IL-1β secretion was enhanced by the pharmacological blockade of autophagosome formation by 3-methyladenine (3-MA) (fig. S7C). As controls, a pan-caspase inhibitor (Z-VAD-FMK) and a caspase-1 inhibitor (YVAD-CHO) both reduced IL-1β secretion (fig. S7C). Thus, inflammasome puncta formed at the MTOC are regulated by autophagy.

HDAC6 deficiency compromised activation of the pyrin inflammasome, but not the AIM2, NLRC4, and noncanonical inflammasomes

Consistent with the MTOC localization and the effects of HDAC6 inhibitors, pyrin inflammasome activation was compromised by knocking out *Hdac6*. This was evident in terms of caspase-1 cleavage, PI staining, IL-1β secretion, and puncta formation (Fig. 4, A to C, and movies S19 and S20). By contrast, dsDNA-induced AIM2 inflammasome activation in *Hdac6*$^{-/-}$ iBMDMs was similar to that in WT controls (Fig. 4, E to H). Reconstitution of WT and mutant human *HDAC6* into *Hdac6*$^{-/-}$ iBMDMs revealed that pyrin inflammasome

Downloaded from http://science.sciencemag.org/ on September 18, 2020

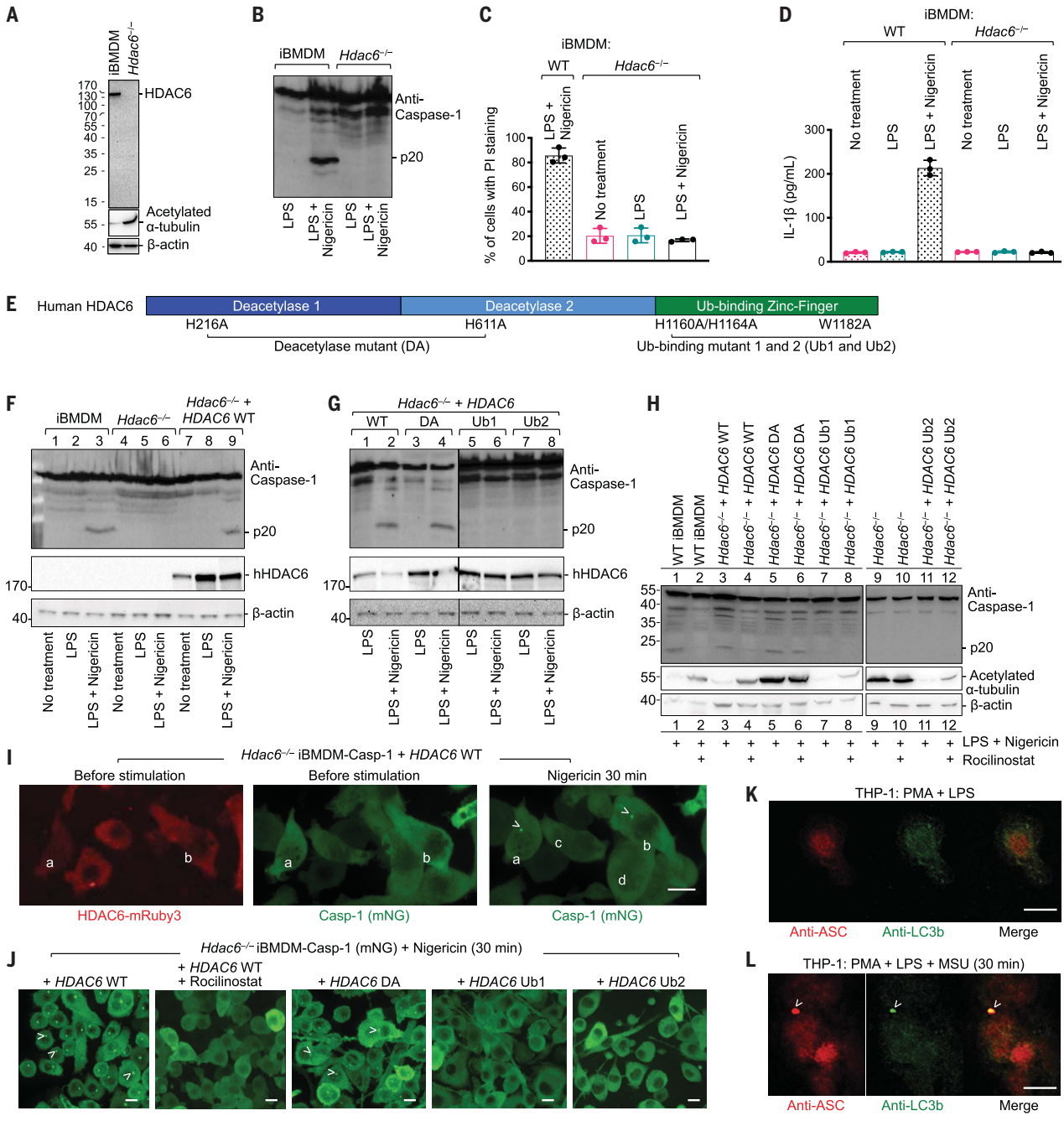

Fig. 3. HDAC6 is required for NLRP3 inflammasome activation. (**A**) Immunoblotting showing the absence of HDAC6 protein in CRISPR/Cas9 *Hdac6*$^{-/-}$ iBMDMs compared with WT iBMDMs. Loading control was provided by the anti–β-actin antibody. The loss of HDAC6 leads to an increase in acetylated α-tubulin depicted using anti–acetylated α-tubulin antibody. (**B** to **D**) Compromised NLRP3 inflammasome activation in *Hdac6*$^{-/-}$ iBMDMs challenged with nigericin is shown for caspase-1 processing (B), PI permeability (C), and secreted IL-1β (D). Data are shown as the mean ± SD for triplicate wells from three or more independent experiments in (C) and (D). (**E**) Domain architecture of human HDAC6 with important mutations (DA, Ub1, and Ub2) labeled. DA: H216A/H611A on catalytic residues, deacetylase mutant; Ub1: mutations H1160A/H1164A on zinc-coordinating residues; Ub2: mutation W1182A on the surface that binds ubiquitin. (**F**) Rescue of nigericin-mediated caspase-1 processing in *Hdac6*$^{-/-}$ iBMDMs by reconstituting with WT human HDAC6. (**G**) Analysis of nigericin-mediated caspase-1 processing in *Hdac6*$^{-/-}$ iBMDMs reconstituted with WT HDAC6 and the DA, Ub1 and Ub2 mutants. (**H**) Sensitivity to rocilinostat in *Hdac6*$^{-/-}$ iBMDMs reconstituted with WT HDAC6, but not the DA mutant, as depicted by inhibition of p20 processing. (**I**) Rescue of nigericin-induced punctum formation in *Hdac6*$^{-/-}$ iBMDM–Casp-1 cells transfected with WT HDAC6-mRuby3. Arrowheads indicate puncta. Cells containing puncta had HDAC6 expression [(a) and (b)], whereas cells that do not contain puncta did not have HDAC6 expression [(c) and (d)]. (**J**) Rescue of nigericin-induced punctum formation in *Hdac6*$^{-/-}$ iBMDM–Casp-1 cells stably reconstituted with WT and DA mutant of HDAC6-mRuby3, but not with Ub1 and Ub2 mutants of HDAC6-mRuby3. Arrowheads indicate puncta. HDAC6 WT reconstituted cells failed to form puncta upon pretreatment by rocilinostat. (**K** and **L**) Inflammasome puncta formation and its link to autophagy analyzed by immunofluorescence of ASC and the autophagy marker LC3b before (K) and after (L) NLRP3 inflammasome stimulation. Arrowheads indicate puncta. Images are representative of three or more independent experiments. Scale bars, 10 μm.

Downloaded from http://science.sciencemag.org/ on September 18, 2020

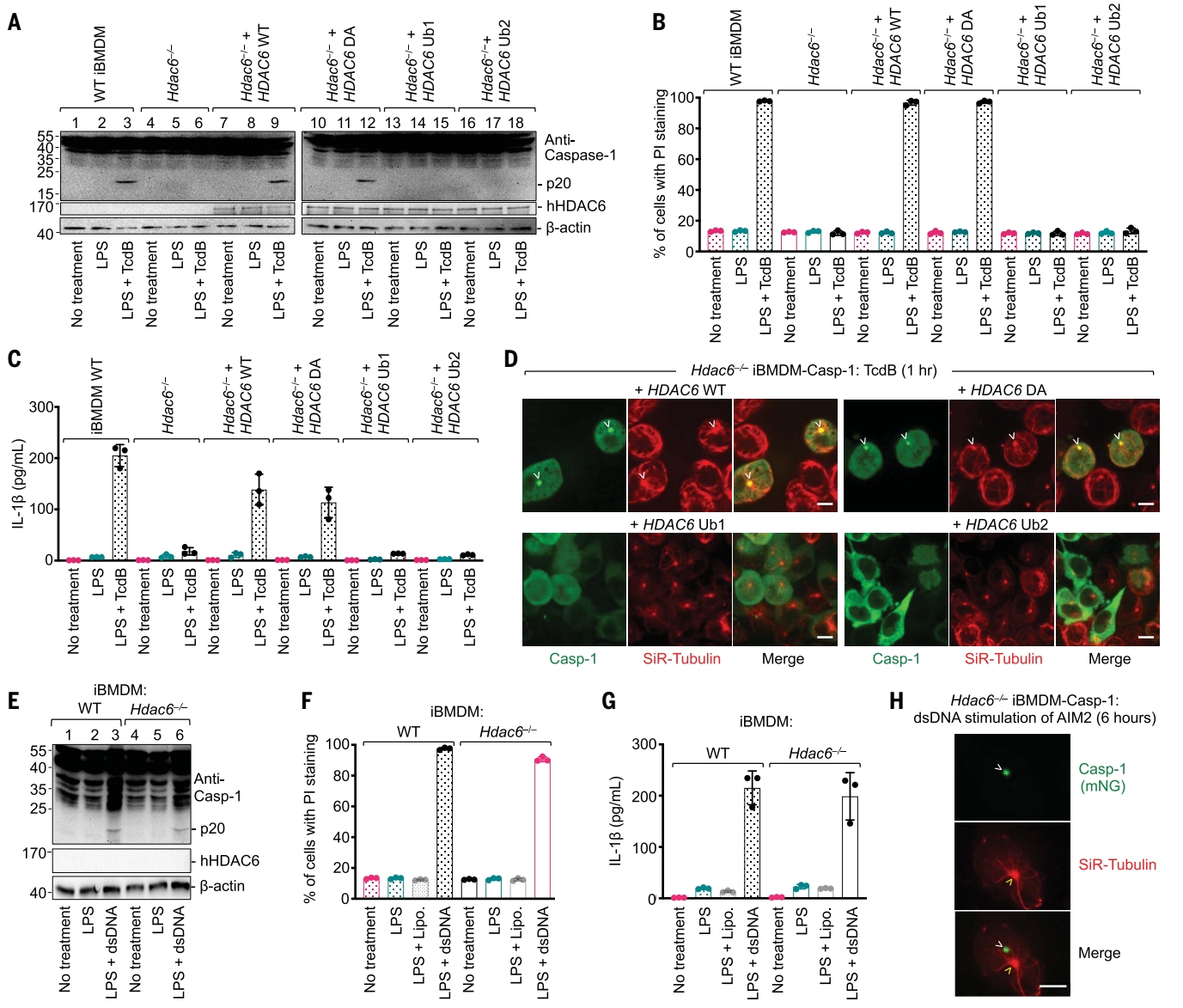

Fig. 4. HDAC6 is required for pyrin inflammasome activation but not AIM2 inflammasome activation. (**A** to **D**) Requirement of HDAC6 and its ubiquitin-binding ability in TcdB-induced pyrin inflammasome activation, as shown by caspase-1 processing (p20) (A), PI permeability (B), IL-1β secretion (C), and punctum formation (D). DA: H216A/H611A on catalytic residues, deacetylase mutant; Ub1: mutations H1160A/H1164A on zinc-coordinating residues; Ub2: mutation W1182A on the surface that binds ubiquitin. (**E** to **H**) Lack of HDAC6 dependence in dsDNA-induced AIM2 inflammasome activation, as shown by caspase-1 processing (p20) (E), PI permeability (F), IL-1β secretion (G), and punctum formation (H). Arrowheads indicate puncta or MTOC. Data are shown as the mean ± SD for triplicate wells from three or more independent experiments [(B), (C), (F), and (G)]. Images are representative of three or more independent experiments [(D) and (H)]. Scale bars, 5 μm.

activation required its intact zinc-finger domain, but not its deacetylase activity, as shown by caspase-1 cleavage (Fig. 4A), PI staining (Fig. 4B), IL-1β secretion (Fig. 4C), and puncta formation (Fig. 4D).

Because the LPS-induced noncanonical inflammasome and the NLRC4 inflammasome are known to induce secondary NLRP3 activation (*47*–*49*), we generated CRISPR/Cas9 knockout of *Hdac6* in the *Nlrp3*$^{-/-}$ background. The noncanonical inflammasome engages mouse caspase-11 in iBMDMs but does not engage caspase-1 for IL-1β processing (*50*, *51*). PI staining indicated equivalent membrane disruption upon LPS transfection in *Nlrp3*$^{-/-}$ and *Nlrp3*$^{-/-}$*Hdac6*$^{-/-}$ iBMDMs (Fig. 5A). The percentage of cells with caspase-11 activity was similar in *Nlrp3*$^{-/-}$ and *Nlrp3*$^{-/-}$ *Hdac6*$^{-/-}$ iBMDMs (Fig. 5B). For the NLRC4 inflammasome, we used *Legionella pneumophila* flagellin fused to the N-terminal domain of *Bacillus anthracis* lethal factor (FlaTox) (*52*). Inactive FlaTox that only engages TLR5 but not NAIP5 was used as a negative control. FlaTox induced comparable caspase-1 processing and PI permeability in *Nlrp3*$^{-/-}$ and *Nlrp3*$^{-/-}$*Hdac6*$^{-/-}$ iBMDMs (Fig. 5, C and D), supporting the notion that HDAC6 is dispensable for activation of the flagellin-NAIP5-NLRC4 inflammasome. NLRC4 inflammasome activation in *Nlrp3*$^{-/-}$ and *Nlrp3*$^{-/-}$*Hdac6*$^{-/-}$ iBMDMs resulted in the formation of ASC puncta, but these puncta did not localize at the MTOC (Fig. 5E). These conclusions were confirmed in mouse primary BMDMs (fig. S19). Thus, HDAC6 only plays a role in inflammasomes

Downloaded from http://science.sciencemag.org/ on September 18, 2020

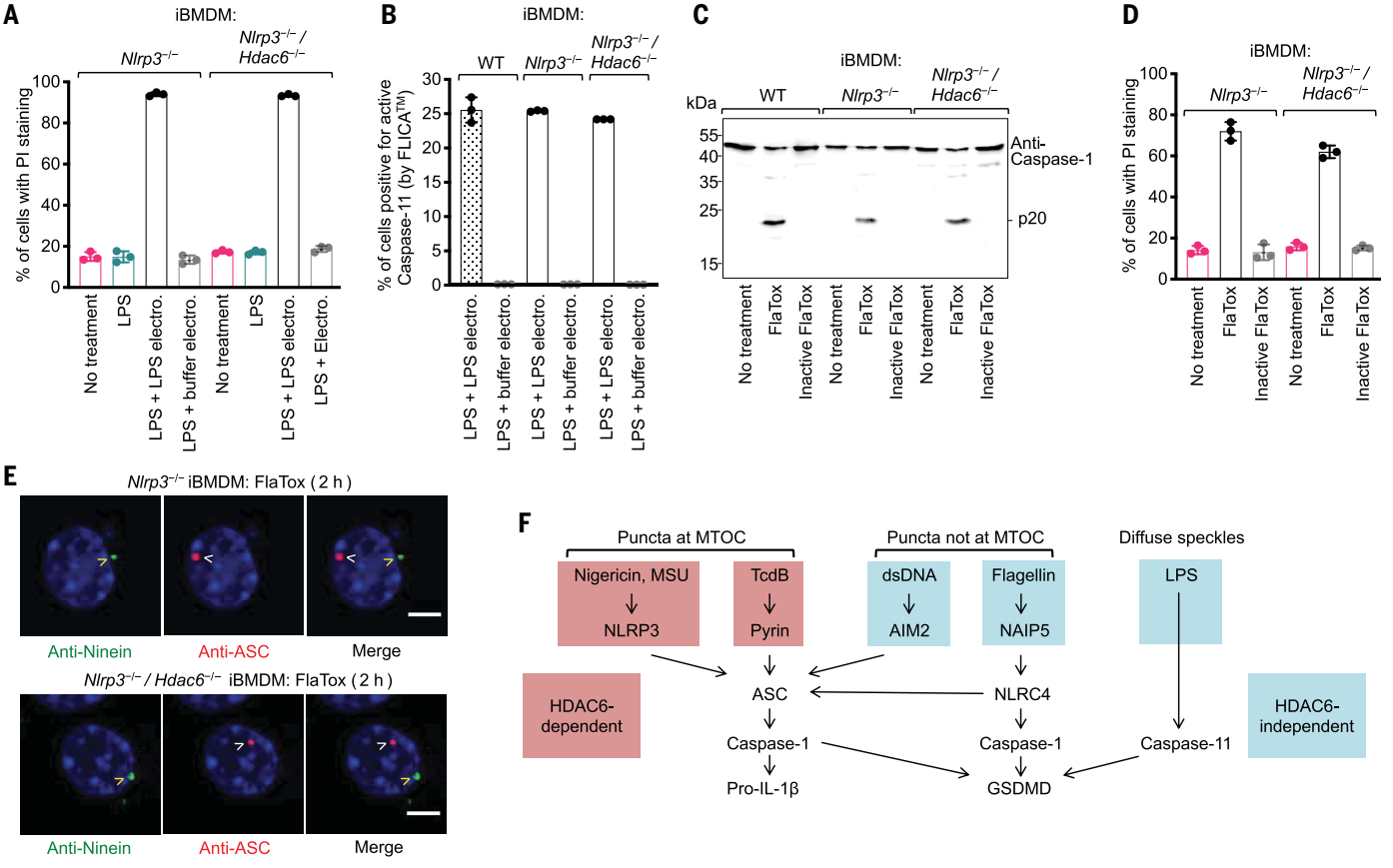

Fig. 5. HDAC6 deficiency does not affect noncanonical and NLRC4 inflammasome activation in an *Nlrp3*$^{-/-}$ background. (**A** and **B**) Noncanonical inflammasome activated by intracellular delivery of LPS (electroporation) quantified by PI permeability (A) and FAM-FLICA substrate cleavage by active caspase-11 (B). (**C** and **D**) NLRC4 inflammasome activation triggered by active FlaTox (inactive FlaTox served as a control) analyzed for caspase-1 processing (p20) (C) and PI permeability (D). Data are shown as the mean ± SD for triplicate wells from three or more independent experiments. (**E**) Immunofluorescence analysis of NLRC4 punctum formation in *Nlrp3*$^{-/-}$ (top) and *Nlrp3*$^{-/-}$*Hdac6*$^{-/-}$ (bottom) iBMDMs upon treatment with FlaTox. Blue represents nuclear staining by Hoechst 33342. The NLRC4 inflammasome punctum represented by ASC staining is distinctly separated from the centrosomal marker ninein. Arrowheads depict puncta or MTOC. Images are representative of three or more independent experiments. Scale bars, 5 μm. (**F**) Summary of location of punctum formation and HDAC6 dependence in the different inflammasomes.

formed at the MTOC, as shown for NLRP3 and pyrin inflammasomes, but not for AIM2 and NLRC4 inflammasomes or the noncanonical inflammasome (Fig. 5F).

HDAC6 is required for transport of TGN-localized NLRP3

Diverse NLRP3 stimuli have been shown to disperse the trans-Golgi network (TGN), which recruits NLRP3 into multiple small speckles before ASC engagement (*53*). We observed partial colocalization between the TGN marker TGN38 and multiple NLRP3 speckles in *Asc*$^{-/-}$ iBMDMs after nigericin stimulation (Fig. 6A). Unexpectedly, in WT iBMDMs, TGN38 redistributed into a single punctum at the MTOC, which colocalized with the NLRP3 single punctum (Fig. 6B). This suggests that NLRP3 is transported by the dynein machinery while on TGN-derived vesicles. By contrast, in *Hdac6*$^{-/-}$ iBMDMs, NLRP3 showed multiple speckles similar to the TGN pattern observed in ASC$^{-/-}$ iBMDMs (Fig. 6C), confirming that HDAC6 is required for the transport. NEK7 is required for NLRP3 activation (*14*–*16*), likely by bridging NLRP3 subunits in an inflammasome disk (*54*). However, NEK7 did not colocalize with NLRP3 at the TGN before HDAC6-mediated microtubule transport (Fig. 6D). This suggests that such transport may be required in NLRP3 activation to bring NLRP3 to the MTOC, where NEK7 resides. Subsequently, activated NLRP3 may nucleate ASC filament formation, which in turn recruits and activates caspase-1 to execute inflammasome effector functions.

HDAC6 is required for LPS- and MSU-induced inflammation in mice

To gain insights into the role of HDAC6 in vivo, we investigated an LPS-induced endotoxic shock model in mice using *Hdac6* deficiency and the HDAC6 inhibitor tubastatin A, as well as the NLRP3 inhibitor MCC950 (*36*). This model was chosen because it is known to engage secondary NLRP3 activation (*55*, *56*) (Fig. 7, A to F, and fig. S20, A to H). Serum IL-1β levels were decreased in mice challenged with LPS but treated with tubastatin A or MCC950 compared with mice challenged with LPS alone (Fig. 7, B and D). IL-18 and TNFα levels were also significantly reduced by tubastatin A or MCC950 treatment (fig. S20, A, C, and D). Harvested lung tissue showed less damage, such as septal mononuclear cell and lymphocyte infiltration, alveolar macrophage and neutrophil infiltration, and alveolar edema, in both the tubastatin A- and MCC950-treated groups, with a significantly reduced overall acute lung injury (ALI) score (Fig. 7, E and F, and fig. S20, G and H). Substantially decreased LPS-induced secretion of IL-1β and IL-18 and ALI were also recapitulated in *Hdac6*$^{-/-}$ mice compared with WT mice (Fig. 7C and fig. S20, B, E, and F). Collectively, these data support the requirement of HDAC6 in NLRP3 inflammasome activation in vivo.

To test a direct NLRP3 activation model, we used the bona fide NLRP3 stimulus MSU to induce peritonitis in mice (Fig. 7G). Consistent with the role of HDAC6 in the NLRP3

Downloaded from http://science.sciencemag.org/ on September 18, 2020

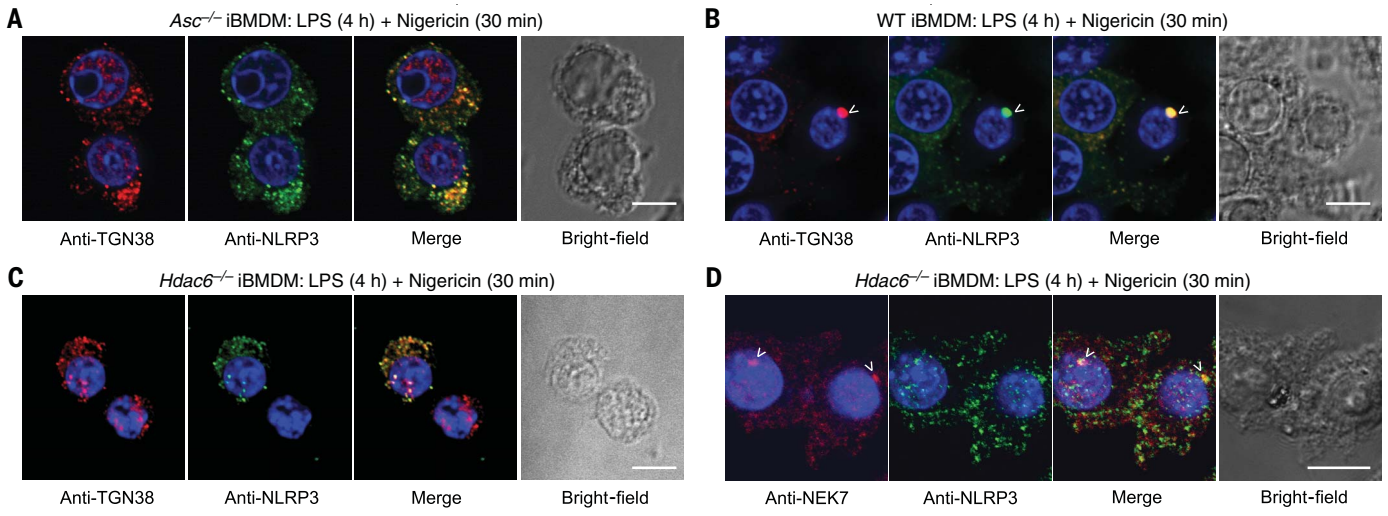

Fig. 6. HDAC6 mediates microtubule transport of TGN-localized NLRP3. (**A** to **C**) Immunofluorescence analysis of TGN38 and NLRP3 in *Asc*$^{-/-}$ iBMDMs (A), WT iBMDMs (B), and *Hdac6*$^{-/-}$ iBMDMs (C). (**D**) Immunofluorescence analysis of NEK7 and NLRP3 distribution in *Hdac6*$^{-/-}$ iBMDMs. Images are representative of three or more independent experiments containing ~100 cells. Arrowheads depict puncta. Scale bars, 10 μm.

inflammasome, IL-1β and IL-18 secretion and neutrophil numbers in peritoneal lavage were decreased in *Hdac6*$^{-/-}$ mice compared with WT mice (Fig. 7, H and I, and fig. S20I). Treatment of WT mice with MCC950 exerted similar effects on IL-1β secretion and neutrophil recruitment as *Hdac6* deficiency (Fig. 7, J and K). Compared with LPS, MSU only induced minimal IL-18 activation, and MCC950 did not significantly reduce the level of IL-18 (fig. S20J). Additionally, MCC950 treatment in *Hdac6*$^{-/-}$ mice did not further suppress MSU-induced IL-1β and IL-18 secretion and neutrophil recruitment (Fig. 7, H and I, and fig. S20I). Thus, we have provided additional further evidence that NLRP3 inflammasome activation depends on HDAC6 in vivo.

Discussion

Our studies support the marked mechanistic parallel between NLRP3 and pyrin inflammasome assembly and HDAC6-mediated transport of pathological aggregates to the MTOC for aggresome formation and degradation. Our results provide insights into the ever-evolving understanding of the complex process of inflammasome activation. They especially offer a framework to integrate the previously implicated role of the microtubule in inflammasome biology, including the importance of the centrosomal protein NEK7 and the microtubule-affinity regulating kinase 4 (MARK4) (*14*, *15*, *57*). The correlation between MTOC localization and sensitivity to microtubule transport disruption among inflammasomes further demonstrates the specificity of the mechanism and points to the importance of the physiological sites of assembly for their activation and regulation in cells (Fig. 5F). The microtubule polymerization inhibitor colchicine is an approved drug used for both gout, an NLRP3 inflammasome disease, and familial Mediterranean fever, a pyrin inflammasome disease. Furthermore, the intermediate filament vimentin, an aggresome component, was shown to regulate NLRP3 inflammasome activation (*22*, *55*). The additional role of the MTOC in inflammasome biology extends its previously established role in directional secretion by T cells at the immune synapse in adaptive immunity (*58*) to innate immunity.

Our data support a model of NLRP3 and pyrin inflammasome activation that depends on regulated ubiquitination (*27*–*30*) and engagement of the dynein adapter HDAC6 and possibly cargo adaptors such as p62. We do not yet know exactly which inflammasome components need to be ubiquitinated. Most likely, NLRP3 is not the inflammasome component recognized by the HDAC6-dynein machinery because the small NLRP3 clusters formed in the absence of ASC are not transported to assemble into one large punctum (*53*). ASC expression, however, leads to the formation of a single punctum per cell (*59*), and both NLRP3 and pyrin are ASC-dependent inflammasomes; critical ubiquitination sites on ASC and IL-1β have been mapped (*27*, *29*). Because NLRP3 is already partially aggregated on the TGN, we hypothesize that small speckles of partially assembled inflammasomes are transported on TGN vesicles.

Why do some inflammasomes form at the MTOC? It is possible that the accumulated focal concentrations promote inflammasome assembly and caspase-1 activation. In the case of NLRP3, its MTOC targeting may ensure engagement of the upstream activator NEK7, a centrosomal kinase (*14*–*16*, *54*). We further resolved that IL-1β conversion also occurs at the MTOC, which although unexpected, is consistent with the recent finding that caspase-1 activity is most dominant at the puncta (*60*). Therefore, site-specific higher-order inflammasome complexes act as supramolecular organizing centers (*61*) to orchestrate inflammasome signaling. The flip side of MTOC localization may be the facilitation of autophagosome formation as a built-in checkpoint mechanism for inflammasome destruction to avoid unrestrained activation. The pericentriolar region is enriched in lysosomes (*62*), and the MTOC acts as a hub to promote the fusion of autophagosomes with lysosomes to accelerate inflammasome degradation. Thus, our data suggest that MTOC localization plays dual activating and inhibiting roles to achieve balanced inflammasome regulation. Although further mechanistic details of this model remain to be elucidated, our studies have clearly identified HDAC6 as a potential therapeutic target for inflammasome-associated diseases.

Materials and methods

Cloning and mutagenesis

The cDNA for human *IL-1B* was a generous gift from J. Yuan, Harvard Medical School. To construct the FRET reporters for IL-1β and caspase-1, the full-length inserts were amplified and ligated into the mTurquoise2-C1 plasmid (a gift from M. Davidson, Addgene no. 54842) between the XhoI and BamHI sites to yield mTurquoise2–IL-1β and mTurquoise2–Casp-1 with a SGLRSRG linker sequence. These constructs then were sub-cloned into the pLV–enhanced GFP (eGFP) lentiviral expression plasmid (a gift from P. Tsoulfas, Addgene no. 36083) between the XbaI and BamHI sites to yield mTurquoise2–IL-1β–eGFP and mTurquoise2–Casp-1–eGFP fusion proteins. Finally, eGFP was

Downloaded from http://science.sciencemag.org/ on September 18, 2020

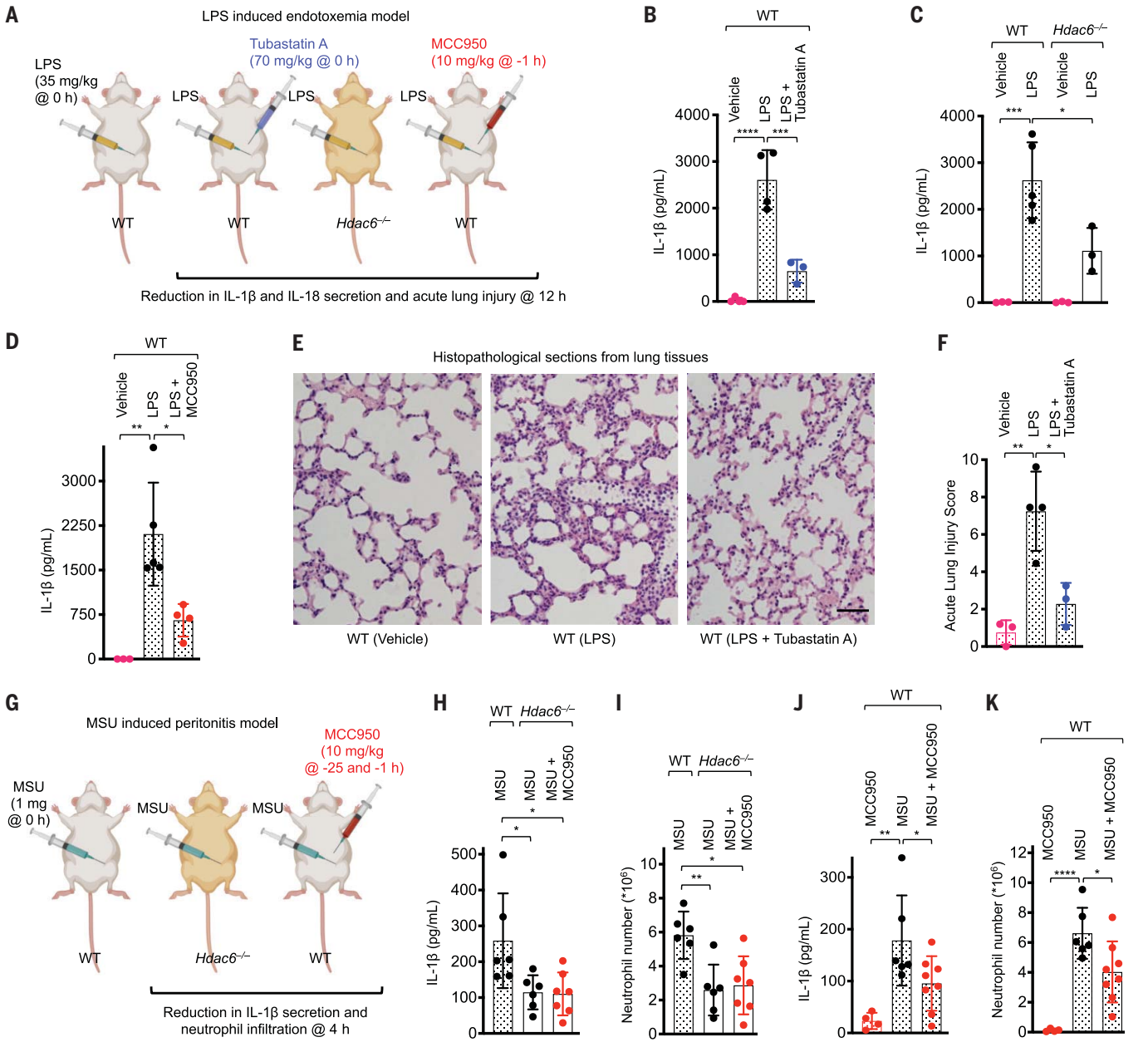

Fig. 7. HDAC6 is required for NLRP3 inflammasome activation in mice. (**A** to **F**) Mouse model of lethal LPS-induced endotoxemia. (A) Experimental layout with indicated timing and dose. (B to D) Effects of tubastatin A (HDAC6 inhibitor) (B), *Hdac6*$^{-/-}$ (C), or MCC950 (NLRP3 inhibitor) (D) on IL-1β secretion. Data are shown as mean ± SD (n = 3 to 5/group). (E) Effects of tubastatin A on ALI. Representative histopathological images from harvested lung tissues are shown. Scale bar, 50 μm. (F) Quantified lung injury depicted by defined clinical parameters in ALI score. ALI scores are shown as mean ± SD (n = 3 to 4/group). (**G** to **K**) Mouse model of MSU-induced peritonitis. (G) Experimental layout with indicted timing and dose. (H and I) Effects of *Hdac6*$^{-/-}$ or *Hdac6*$^{-/-}$ + MCC950 on peritoneal IL-1β production (H) and neutrophil recruitment (I) upon MSU challenge. Data are shown as mean ± SD (n = 6 to 7/group). (J and K) Effects of MCC950 on peritoneal IL-1β production (J) and neutrophil recruitment (K) upon MSU challenge. Data are shown as mean ± SD (n = 5 to 8/group). For (B) to (D), (F), and (H) to (K), analysis of variance (ANOVA) followed by Bonferroni's multiple-comparisons test was performed for data analysis as used previously (*66*, *67*). *$P \le 0.05$, **$P \le 0.01$, ***$P \le 0.001$, and ****$P \le 0.0001$.

replaced with mNeonGreen (mNG) with an engineered linker sequence of TGSGS between the AgeI and SalI sites using the following primers (Integrated DNA Technologies) to generate the mTurquoise2–IL-1β–mNG and mTurquoise2–Casp-1–mNG constructs: forward primer of 5′-GATGCAACCGGTAGCGGCTCAATGGTGAGCAAGGGCGAG-3′ and reverse primer of 5′-GATGCAGTCGACTTACTTGTACAGCTCGTC-3′.

The mRuby3-Dynamitin (p50) fusion construct was produced by first inserting mRuby3 into the pLV-eGFP plasmid between the XbaI and BamHI sites. Then, the full-length dynamitin insert was amplified and ligated between the AgeI and SalI sites from the cDNA (a gift from I. Cheeseman, Addgene no. 37388) using the following primers (Integrated DNA Technologies): forward primer of 5′-GATGCAACCGGTGGCGGCCGCTC-3′ and reverse primer of 5′-GATGCAGTCGACTCACTTTCCCAGCTTC-3′.

Downloaded from http://science.sciencemag.org/ on September 18, 2020

The HDAC6-Flag-mRuby3 fusion construct was made by first subcloning mRuby3 into the pLV-eGFP plasmid between the AgeI and SalI sites to yield pLV-mRuby3, followed by amplifying HDAC6-Flag from the cDNA (P. Matthias) and ligating between XbaI and AgeI sites to yield HDAC6-Flag-mRuby3. The following primers were used (Integrated DNA Technologies): forward primer of 5′-GATGCATCTAGAATGACCTCAACCGGCC-3′ and reverse primer of 5′-GATGCAACCGGTCTTGTCATCGTCGTCC-3′.

The HDAC6 deacetylase mutant (DA, H216A/H611A) was produced similarly as above except with the plasmid pcDNA-HDAC6.DC-Flag (a gift from T.-P. Yao, Addgene no. 30483). The ubiquitin-binding mutants Ub1 (H1160A/H1164A) and Ub2 (W1182A) were produced by site-directed mutagenesis using the QuikChange Lightning Multi kit (Agilent Technologies) with the following primers (Integrated DNA Technologies): Ub1 forward primer: 5′-GTCGTTACATCAATGGCGCCATGCTCCAAGCCCATGGAAATTCTGGAC-3′; Ub1 reverse primer: 5′-GTCCAGAATTTCCATGGGCTTGGAGCATGGCGCCATTGATGTAACGAC-3′; Ub2 forward primer: 5′-CATCGACCTGTCAGCCCGTGTTACTACTGTCAGG-3′; and Ub2 reverse primer: 5′-CCTGACAGTAGTAACACGCGGCTGACAGTCGATG-3′.

The GTU-eGFP construct was produced similarly as above except that it was cloned in the plasmid pLV-eGFP (a gift from P. Tsoulfas, Addgene no. 36083). Before cloning, the existing XbaI site was mutated to NheI site in the plasmid. The human GTU insert was amplified using mRuby-Gamma-Tubulin-17 as a template (a gift from M. Davidson, Addgene no. 55864) using the following primers (Integrated DNA Technologies): forward primer of 5′-TTTTGCTAGCTGCCACCATGCCGAGGGAAATCATCA-3′ and reverse primer of 5′-TTTTACCGGTTTCTGCTCCTGGGTGCCC-3′.

pENTR221 mASC-tagRFP-T was generated by a BP gateway recombination reaction of pDONR221 with the PCR product attB1_mASC-tagRFP-T_attB2, catalyzed by BP clonase II (Thermo Fisher Scientific) according to the manufacturer's recommendations. Mouse ASC and tagRFP-T (*63*) coding sequences are connected by the linker SGGRSSGSGSTSGSG. pRRL mASC-tagRFP-T puro was generated by three-fragment gateway recombination of pRRL R4-R3 Puro with pENTR L4-R1 pMT (mouse metallothionein I promoter), pENTR221 mASC-EGFP, and pENTR R2-L3 STOP MCS using LR Clonase II Plus enzyme (Thermo Fisher Scientific). Vectors were kind gifts from S. Lindquist (Whitehead Institute for Biomedical Research, Cambridge, MA, USA).

Human ASC was subcloned into the pLV-mRuby3 plasmid (described previously) between the XbaI and AgeI sites using the following primers (Integrated DNA Technologies): forward primer of 5′-GATGCATCTAGAATGGGGCGCGCGCGCG-3′ and reverse primer of 5′-GATGCAACCGGTGGATCCGCTTCCGCTCCGCTCCAGGTCC-3′. This resulted in pLV-ASC-mRuby3 with a short linker GSGSTGSAS between ASC and mRuby3. The full-length human Flag-ASC cDNA was generated by inserting the full-length human ASC-flag tagged at N terminus in the EcoRI and XhoI sites of plenti-CAG-IRES-GFP (a gift from W. Kaelin, Addgene no. 69047) using the following primers (Integrated DNA Technologies): forward primer of 5′-TGTGCTGTCTCATCATTTGGCAAAGAATTCGACTACAAAGACGATGACGACAAG-3′ and reverse primer of 5′-CCAGTAACGTTAGGGGGGGGGCGGAATTGATCCCGCTCGAGTCAGCTCCGCTCCAGGTCCTCCACC-3′.

pET15b LFn-Fla and LFn-Fla 3A fusion constructs were a gift from R. Vance (Addgene no. 84871 and 84872, respectively).

Cell culture and transfection

iBMDMs from WT C57BL/6 mice were a gift from Prof. J. Kagan (Boston Children's Hospital, Boston, MA, USA). Immortalized *Asc*$^{-/-}$, *Nlrp3*$^{-/-}$, *Casp-1/11*$^{-/-}$ deficient macrophages were a gift from Prof. K. A. Fitzgerald (University of Massachusetts Medical School, Worcester, MA, USA). Immortalized *Nek7*$^{-/-}$ macrophages were a gift from Prof. G. Nuñez (University of Michigan, Ann Arbor, MI, USA).

HEK293T and iBMDMs were grown in Dulbecco's modified Eagle's medium (DMEM), with L-glutamine (Thermo Fisher Scientific, catalog no. 10569-004), supplemented with 10% fetal bovine serum (FBS) (Thermo Fisher Scientific, catalog no. 16000-044). Human monocytic THP-1 cells were maintained in Roswell Park Memorial Institute medium with L-glutamine (Thermo Fisher Scientific, catalog no. 11835-055) supplemented with 10% FBS and 0.05 mM 2-mercaptoethanol (Sigma-Aldrich, catalog no. D2650-100ML). Newly thawed HEK-Blue IL-1β cells were first grown in growth medium containing DMEM with L-glutamine, supplemented with heat-inactivated 10% FBS, 50 U/ml penicillin, 50 μg/ml streptomycin (Thermo Fisher Scientific, catalog no. 15140-163), and 100 μg/ml Normocin (Invivogen, catalog no. ant-nr-1). After two passages, the cells were grown in selective medium containing DMEM with L-glutamine, supplemented with heat inactivated 10% FBS, 100 μg/ml zeocin (Invivogen, catalog no. ant-zn-1), 200 μg/ml hygromycin B (Invivogen, catalog no. ant-hg-1), 50 U/ml penicillin, 50 μg/ml streptomycin, and 100 μg/ml Normocin. For preparation of L929-conditioned medium, 5×10^5 L929 cells were grown in a 75-cm^2 flask containing 50 ml of DMEM. Supernatant was collected on day 7 and passed through a 0.45-μm filter. The 25-ml aliquots of L929-conditioned medium were stored at −80°C.

All cells were maintained at 37°C with 5% CO_2. For inflammasome activation studies, THP-1 cells were treated overnight with 300 ng/ml phorbol myristate acetate (Sigma-Aldrich, catalog no. P8139-5MG), followed by 4 hours of priming with 1 μg/ml LPS (Invivogen, catalog no. tlrl-b5lps). iBMDMs were primed for 4 hours with LPS. The following activators were used for inflammasome studies: 200 μg/ml MSU crystals (Santa Cruz Biotechnology, catalog no. sc-202711), 20 μM nigericin (Sigma-Aldrich, catalog no. N7143-5MG), 5 mM ATP (Sigma-Aldrich, catalog no. FLAAS-1VL), 100 μg/ml alum (Invivogen, catalog no. tlrl-alk), and 100 μg/ml Nano-SiO_2 (Invivogen, catalog no. tlrl-sio) for NLRP3 inflammasome activation; 0.5 μg/ml TcdB for pyrin inflammasome activation; 1 μg/ml dsDNA (Sigma-Aldrich, catalog no. P0883-25UN) for AIM2 inflammasome activation for the indicated time intervals; and active and inactive FlaTox (2 μg/ml) in combination with protective antigen (2 μg/ml) (List Biological Laboratories Inc., catalog no. 171E) for NLRC4 inflammasome activation.

For live-cell and-fixed cell confocal microscopy, cells were grown in microwell dishes (MatTek, catalog no. P35G-1.5-14-C). Transfection was performed at 60% confluency using linear PEI (MW 25,000; Polysciences Inc., catalog no. 23966-2) or FuGENE 6 (Promega, catalog no. E2691) according to the manufacturer's guidelines.

Generation of stable cell lines

To generate stable cell lines, on day 0, lentivirus was produced using human embryonic kidney 293T (HEK293T) cells by cotransfecting 1 μg of pLV plasmid containing the gene, 750 ng of psPAX2 packaging plasmid, and 250 ng of pMD2.G envelope plasmid (both plasmids were a gift from D. Trono, Addgene no. 12260 and 12259, respectively). The transfected cells were incubated overnight. The following day (day 1), the medium was removed and the cells were replenished with 1 ml of fresh medium and incubated for another day. On day 2, the supernatant containing the virus was filtered using a 0.45-μm filter (Pall Corporation, catalog no. 4184) and used directly to infect iBMDMs with a spinfection protocol to increase the efficacy. Spinfection was performed at 2500*g* for 90 min at room temperature using 8 μg/ml polybrene (Santa Cruz Biotechnology, catalog no. sc-134220). After spinfection, cells were further incubated for the expression of marker genes to identify the positive clones. Positive clones were selected either by cell sorting or antibiotic selection, and colonies were expanded from single clones. Positive clones were extensively validated by PCR, immunoblotting, and immunofluorescence microscopy.

FACS

Fluorescence-activated cell sorting (FACS) was performed using a FACSAria II cell sorter

Downloaded from http://science.sciencemag.org/ on September 18, 2020

from BD Biosciences equipped with FACSDiva version 8.03. The instrument was set up with a 100-μm nozzle at 20 psi, and the samples were introduced to the system at the lowest flow rate to minimize shear stress. The sorted populations were gated to exclude double, dead, and autofluorescent cells. The sort was performed with a purity precision mode.

Pharmacological inhibition

LPS-primed iBMDMs were pretreated for 1 hour with the HDAC6 inhibitors tubastatin A (10 μM; Sigma-Aldrich, catalog no. SML0044), rocilinostat (30 μM; Selleckchem, catalog no. S8001), or tubacin (20 μM or 5 to 40 μM; Enzo Life Sciences, catalog no. BML-GR362-0500), with the microtubule polymerization inhibitors colchicine (10 μM; Sigma-Aldrich, catalog no. C9754-100MG) or nocodazole (10 μM; Sigma-Aldrich, catalog no. M1404-2MG), or with the NLRP3 inhibitor MCC950 (0.1 to 20 μM; CP-456773; Cayman Chemicals, catalog no. 210826-40-7, and Sigma-Aldrich, catalog no. PZ0280). Cytoplasmic dynein-dependent microtubule transport was inhibited using 25 μM ciliobrevin A (TOCRIS Bioscience, catalog no. 4529). One hour after drug pretreatment, activation was performed either with nigericin (30 min), dsDNA (6 hours), or TcdB (1 hour). iBMDMs were pretreated with 5 mM 3-MA (Invivogen, catalog no. tlrl-3ma) for 6 hours to block autophagy.

Measurement of membrane disruption by PI-assisted flow cytometry

Membrane permeability was measured by PI exclusion assay. Untreated and treated cells were collected, including dead floating cells in the medium, and washed two times in PBS before resuspension in 2 μg/ml PI (Immunochemistry Technologies, catalog no. 638). The percentage of cells that took up PI was measured by flow cytometry (BD Biosciences, FACSAria II).

Detection of IL-1β by reporter HEK-Blue IL-1β cells

Procedures were performed according to manufacturer's instructions (Invivogen). Briefly, HEK-Blue IL-1β cells grown to 60% confluence were seeded on a flat-bottom, 96-well plate at ~50,000 cells per well. These cells were incubated overnight with 50 μl of activated THP-1 or iBMDM supernatant along with the corresponding controls at 37°C in 5% CO_2. The supernatants from the induced HEK-Blue IL-1β cells were collected for the soluble embryonic alkaline phosphatase assay (SEAP) using QUANTI-Blue (Invivogen, catalog no. repqb1). In this colorimetric assay, 150 μl of resuspended QUANTI-Blue was incubated with 50 μl of induced HEK-Blue™ IL-1β cell supernatant in a flat-bottom 96-well plate at 37°C from 30 min to 3 hours. SEAP levels were read at 650 nm. The graphs were plotted using GraphPad Prism 7 software.

Detection of cytokines by ELISA

Detection kits for mouse IL-1β (Affymetrix eBioscience, catalog no. 88-7013; R&D Systems, catalog no. DY401), mouse TNFα (Invitrogen, catalog no. BMS607HS; R&D Systems, catalog no. DY410), mouse IL-18 (Thermo Fisher Scientific, catalog no. BMS618-3), and human IL-1β (BD Biosciences, catalog no. 557953) were used at the specified temperature and conditions according to the manufacturer's instructions. IL-18 concentration was also measured using sandwich enzyme linked immunosorbent assay (ELISA) with capture antibody: 500 ng/ml of mouse anti–IL-18 (MBL, catalog no. D047-3), standard (MBL, catalog no. B002-5), and biotinylated detecting antibody (MBL, catalog no. D048-6) at the Cancer Center Immunology Core at the University of Michigan.

Spinning-disk confocal live-cell microscopy

Sorted cells were grown in 35-mm petri dishes (10-mm microwell, no. 1.5 coverglass, MatTek, catalog no. P35G-1.5-14-C) and mounted in a 20/20 Technologies Bionomic microscope stage heated chamber warmed to 37°C. DMEM without phenol red (Thermo Fisher Scientific, catalog no. 21063-045) was used during image acquisition, with a layer of mineral oil on top of the medium to prevent evaporation. All images were collected with a Yokogawa spinning-disk confocal on a Nikon Ti inverted microscope equipped with Plan Apo phase 3 oil-immersion 40× (1.3 numerical aperture) and oil-immersion 60× (1.4 numerical aperture) lenses. The Perfect Focus System was in place for continuous maintenance of focus. IL-1β and caspase-1 mNG fluorescence was excited with a 491-nm line (selected with a 488/10 filter, Chroma, catalog no. 53044) from a 100mW cobalt diode laser and collected with a quadruple band pass dichroic mirror (Chroma, catalog no. 89100bs) and a 525/50 emission filter (Chroma, catalog no. 53051). Human HDAC6-mRuby3 and p50 dynamitin-mRuby3 fluorescence were excited with a 561-nm line 200-mW cobalt diode laser and collected with a quadruple band-pass dichroic mirror (Chroma, catalog no. 89100bs) and a 620/60 emission filter. SiR-Tubulin fluorescence was excited with a 642-nm line from a 101-mW cobalt diode laser and collected with a quadruple band-pass dichroic mirror (Chroma, catalog no. 89100bs) and a 700/75 emission filter (Chroma, catalog no. ET700/75m). Before acquisition, cells were primed with LPS for 4 hours, followed by activation using nigericin, MSU, and ATP for 30 min; alum and Nano-SiO_2 for 6 hours; TcdB for 1 hour; or dsDNA for 6 hours. SiR-Tubulin incubation was performed for 4 hours (Cytoskeleton, catalog no. CY-SC006 with 1 μM SiR-Tubulin and 10 μM verapamil) to stain the microtubule network in live cells.

Images were acquired with a Hamamatsu ORCA ER cooled CCD camera controlled with MetaMorph version 7 software. Images were collected using an exposure time of 700 ms and 2 × 2 binning, with illumination light shuttered between acquisitions. At each time point, *z*-series optical sections were collected with a step size of 1 μm for the indicated time intervals using a Prior Proscan focus motor. Gamma, brightness, and contrast were adjusted on displayed images (identically for comparative image sets) using MetaMorph version 7 software.

Confocal laser-scanning microscopy

For imaging fixed cells, THP-1 cells or iBMDMs were seeded at a density of 2×10^5/ml. Eight to 12 hours after transfection, HEK293T cells were washed once with 1× BRB80 buffer, fixed, and analyzed by immunofluorescence microscopy. After activation, THP-1 and iBMDMs were washed once with 1× BRB buffer, fixed, and labeled with antibodies, as described in the immunolabeling and antibodies section. Confocal sections were obtained using an Olympus FV-1000 laser-scanning confocal microscope (Olympus America, Waltham, MA) with Olympus Fluoview version 3.0 software, using 405-nm excitation/425- to 475-nm emission, 488-nm excitation/500- to 545-nm emission, 559-nm excitation/575- to 620-nm emission, and 635-nm excitation/655- to 755-nm emission laser lines.

Images (512 × 512 or 1024 × 1024) were collected at 4 μs/pixel using a 20× [0.75 numerical aperture (NA), air objective], 40× (0.95 NA, air objective), 40× (1.15 NA, water-immersion objective), or 60× (1.2 NA, water-immersion objective) lenses. The images were identically acquired and processed using Adobe Photoshop software. Distributions of fluorescence intensities and colocalization were analyzed by Velocity version 6.2.1 software.

LLSM

iBMDM–IL-1β cells stably expressing mTurquoise2–pro-IL-1β–mNG were plated on 5-mm round glass coverslips and stained with SiR-Tubulin. These coverslips were picked up with forceps and placed in the sample bath of the 3D LLSM (*18*). The sample was imaged in two ways. First, it was imaged in a time series in 3D using a dithered multi-Bessel lattice light-sheet by stepping the sample stage at 500-nm intervals in the *s*-axis equivalent to an ~261-nm translation in the *z*-axis. Thus, each 3D image took 450 ms to acquire for a total of 90 time points. Each 3D stack corresponded to a predeskewed volume of ~30 μm × 50 μm × 4 μm (300 × 512 × 15 pixels). The cell was excited with a 488-nm laser (~300-mW operating power with an illumination of ~400 μW at the back aperture) and a 642-nm laser (~100-mW operating power

Downloaded from http://science.sciencemag.org/ on September 18, 2020

with an illumination of ~200 μW at the back aperture) to acquire 15 imaging planes, each exposed for ~14.8 ms and recorded with two Andor iXon 897 EMCCD cameras. Second, the sample was imaged at a single time point in 3D using a dithered multi-Bessel lattice light-sheet by stepping the sample stage at 250 nm intervals in the *s*-axis equivalent to ~130-nm translation in the *z*-axis. The 3D image required 10 s to acquire. The stack corresponded to a predeskewed volume of ~30 μm × 50 μm × 13 μm (300 × 512 × 100 pixels). The cells were excited with a 488-nm laser (~300-mW operating power with an illumination of ~400 μW at the back aperture) and a 642-nm laser (~15-mW operating power with an illumination of ~30 μW at the back aperture) to acquire 100 imaging planes, each exposed for ~49.8 ms and recorded with two Andor iXon 897 EMCCD cameras. The inner and outer NAs of excitation were 0.35 and 0.4, respectively.

Immunolabeling and antibodies

THP-1 cells or iBMDMs were first primed for 4 hours with LPS and then activated with nigericin, TcdB, or dsDNA for various lengths of time. Fixative, permeabilization, and blocking buffers were prepared in Brinkley buffer 80 (BRB80) and kept at 37°C before use. BRB80 buffer was prepared freshly using 80 mM PIPES, 1 mM $MgCl_2$, and 1 mM EGTA, titrated to pH 6.8 with a saturated solution of KOH.

Cells were fixed in 3.7% paraformaldehyde for 1 to 5 min at room temperature and then washed twice using BRB80 with 5-min intervals between washes. Permeabilization was performed for 5 min at room temperature using 0.15% Triton X-100 (in 1× BRB80). Washing was performed to remove permeabilization buffer. Cells were then blocked for 1 hour at room temperature using blocking buffer (3% gelatin from cold-water fish skin prepared in 1× BRB80). Cells were incubated with primary (3 hours to overnight) and secondary (1 hour) antibodies. Nuclei were stained using Hoechst 33342 (Invitrogen, catalog no. H3750). In between, extensive washing steps were performed to remove unbound antibodies and stains.

To stain for active caspase-1, the carboxyfluorescein (FAM)–labeled inhibitor of caspase-1 (FAM-FLICA) kit (ImmunoChemistry Technologies, catalog no. 97) was used according to the manufacturer's instructions. After NLRP3 activation, the supernatant from macrophages was removed and was replaced with medium containing 1× reconstituted fluorescently labeled inhibitor of active caspase-1 (FAM-FLICA), and incubated for 1 hour. Unbound fluorescent label was aspirated and replaced with regular medium. This washing step using regular medium was performed for 1 hour at 37°C at 5% CO_2. After washing, live cells were fixed in 3.7% paraformaldehyde and stained as described above.

The following primary antibodies were used: anti-ASC (N-15), 1:1000 (rabbit polyclonal, Santa Cruz Biotechnology catalog no. sc-22514-R); anti-ASC (clone 2EI-7), 1:1,000 (mouse monoclonal, EMD Millipore, catalog no. 04-147); anti-ASC (D2W8U), 1:1,000 (rabbit monoclonal, Cell Signaling Technology, catalog no. 67824); anti-GTU, 1:500 (mouse monoclonal, Abcam catalog no. ab11316); anti-ninein (F-5), 1:2000 (goat polyclonal, Santa Cruz Biotechnology, catalog no. sc-376420); anti–pro-IL-1β, 1:1,000 (rabbit polyclonal, Abcam, catalog no. ab104279); anti–pro-IL-1β, 1:1000 (goat polyclonal, R&D Systems, catalog no. AF-401-NA); anti-TGN38, 1:1000 (rabbit polyclonal, Novus Biologicals, catalog no. NBP1-03495SS); anti–IL-1β (H-153), 1:1,000 (rabbit polyclonal, Santa Cruz Biotechnology, catalog no. sc-7884); anti-NLRP3, 1:100 (goat polyclonal, Abcam, catalog no. ab4207); mouse anti–caspase-1 (p20), 1:2000 (mouse monoclonal, Adipogen, catalog no. AG-20B-0042-C100); human anti–caspase-1 (p20), 1:2000 (mouse monoclonal, Adipogen, catalog no. AG-20B-0048-C100); human HDAC6 (D2E5), 1:1000 (rabbit monoclonal, Cell Signaling Technology, catalog no. 7558S); mouse HDAC6 (D21B10), 1:1000 (rabbit monoclonal, Cell Signaling Technology, catalog no. 7612S); mouse anti-NEK7 (B-5), 1:1000 (mouse monoclonal, Santa Cruz Biotechnology, catalog no. sc-393539); anti-FLAG M2 1:500 (mouse monoclonal, Sigma-Aldrich, catalog no. A2220); rabbit immunoglobulin fraction (normal) (Agilent Dako, catalog no. X0903); goat IgG, polyclonal isotype control (Abcam, catalog no. ab37373); mouse IgG_1 isotype control (R&D Systems, catalog no. MAB002); anti–β-actin 1:5000 (mouse monoclonal, Santa Cruz Biotechnology, catalog no. 47778); anti–acetylated α-tubulin 1:5000 (mouse monoclonal, Sigma-Aldrich, catalog no. T7451); and anti-pyrin 1:1000 (rabbit monoclonal, Abcam, catalog no. ab214772).

The following secondary antibodies were used: Alexa Fluor 488–labeled goat anti-mouse IgG, IgM (H+L) (1:500, Thermo Fisher Scientific, catalog no. A10680); Alexa Fluor 647–labeled goat anti-rabbit IgG (H+L) (1:2000, Thermo Fisher Scientific, catalog no. A21244); Alexa Fluor 568–labeled donkey anti-goat IgG (H+L) (1:1000, Thermo Fisher Scientific, catalog no. A11057); Alexa Fluor 568–labeled goat anti-rabbit IgG (H+L) (1:1000, Thermo Fisher Scientific, catalog no. A11036); Alexa Fluor 647–labeled goat anti-mouse IgG (H+L) (1:1000, Thermo Fisher Scientific, catalog no. A21236); HRP-conjugated goat anti-rabbit IgG (1:10,000, Cell Signaling Technology, catalog no. 7074S); and HRP-conjugated horse anti-mouse IgG (1:10,000, Cell Signaling Technology, catalog no. 7076S).

The recruitment of neutrophils into the peritoneal cavity was analyzed by flow cytometry using Alexa Fluor 488–labeled rat anti-mouse Ly-6G/Ly-6C (Gr-1) IgG (1:200, BioLegend, catalog no. 108417) and Alexa Fluor 700–labeled rat anti-mouse CD45 IgG (1:200, BioLegend, catalog no. 103128).

For the caspase-1 (p20) analysis, the whole cell lysate was prepared in 1× sodium dodecyl sulfate (SDS) sample buffer as described previously (*64*). Lysates were resolved on 12.5% SDS–polyacrylamide gel electrophoresis (PAGE) gel and subjected to immunoblotting using the mouse caspase-1–specific antibodies listed above.

Affinity purification of NEK7 rabbit polyclonal antibodies

NEK7 antibody was a kind gift from K. Rhee of Seoul National University. The NEK7 antibody was affinity purified by incubation of the antiserum with a purified full-length NEK7 blotted on a nitrocellulose strip (SDS-PAGE separated and transferred on a nitrocellulose membrane). Elution was performed on a shaker at 50°C at 500 rpm (Mixer HC, USA Scientific) using 100 mM glycine, pH 2.5. The eluted antibody fraction was neutralized by 1.5 M Tris-HCl, pH 8.8.

Generation of Hdac6 CRISPR-knockout mouse iBMDMs

Two independent *Hdac6* CRISPR-knockout cell lines were generated. The first $Hdac6^{-/-}$ cell line was generated using two guide RNAs (gRNAs) targeting the first coding exon of mouse *Hdac6*. The sequences for mouse *Hdac6* gRNAs were as follows: gRNA#1, sense strand: 5′-AGTAGAAGAATCTTGGCCGG-3′, antisense strand: 5′-CCGGCCAAGATTCTTCTACT-3′; gRNA#2, sense strand: 5′-GTGGGTGATTTTTCTGGGGAA-3′, antisense strand: 5′-TTCCCCAGAAAAATCACCCAC-3′. The second $Hdac6^{-/-}$ cell line was generated using two gRNAs targeting the fourth and eighteenth coding exon of mouse *Hdac6*. The sequences for mouse HDAC6 gRNAs were as follows: gRNA#3, sense strand: 5′-CCTGAGACAAGAGTGCCAGT-3′, antisense strand: 5′-ACTGGCACTCTTGTCTCAGGC-3′; gRNA#4, sense strand: 5′-CAGCGCATCTTACGCATCATC-3′, antisense strand: 5′-ATGATGCGTAAGATGCGCTG-3′.

To clone the gRNA sequences into Lenti-CRISPR vector V2 (a gift from F. Zhang, Addgene no. 52961), the plasmid was cut and dephosphorylated with FastDigest BsmBI (Fermentas, catalog no. FD0454), and FastAP (Fermentas, catalog no. E0651) at 37°C for 2 hours. Oligonucleotides for the mouse HDAC6 gRNA sequences (Integrated DNA Technologies) were annealed by heating to 95°C for 5 min and cooling to 25°C at 1.5°C/min. The sequence of the oligonucleotides used for cloning into the LentiCRISPR vector V2 were as follows: forward primer for gRNA#1: 5′-CACCGAGTAGAAGAATCTTGGCCGG-3′, reverse primer for gRNA#1: 5′-AAACCCGGCCAAGATTCTTCTACTC-3′ and forward primer for gRNA#2:

Downloaded from http://science.sciencemag.org/ on September 18, 2020

5′-CACCGGTGGGTGATTTTTCTGGGGAA-3′, reverse primer for gRNA#2: 5′-AAACTTCCCCAGAAAAATCACCCAC-3′, forward primer for gRNA#3: 5′-CACCGCCTGAGACAAGAGTGCCAGT-3′, reverse primer for gRNA#3: 5′-AAACACTGGCACTCTTGTCTCAGGC-3′ and forward primer for gRNA#4: 5′-CACCGCAGCGCATCTTACGCATCATC-3′, reverse primer for gRNA#4: 5′-AAACATGATGCGTAAGATGCGCTGC-3′. Using T7 ligase (Enzymatics, catalog no. L602L), annealed oligos were ligated into gel-purified vectors at 25°C for 5 min. Cloned transfer plasmids were amplified using an endotoxin-free mini-prep kit (Qiagen, catalog no. 27104). LentiCRISPR vector V2 containing *Hdac6* gRNA was used to generate the virus in HEK293T cells followed by infection of WT mouse iBMDM cell line. Positive infected cells were isolated by puromycin selection (inserted into LentiCRISPR vector V2) at 10 μg/ml (Thermo Fisher Scientific, catalog no. A1113803). Colonies were expanded from single clones and selected for the puromycin resistance. *Hdac6*$^{-/-}$ iBMDMs were analyzed by PCR on genomic DNA and were further validated at the protein and functional levels.

Genomic PCR

Genomic DNA was extracted using the QiaAmp DNA mini kit (Qiagen, catalog no. 13323 according to the manufacturer's instructions, and the knockout phenotype was confirmed by PCR on the first coding exon using following primers (Integrated DNA Technologies): forward primer: 5′-GTGGGGTCTGAAGGATTCTGA-3′; reverse primer: 5′-TCTTGTCTCAGGGTTCAGATC-3′. For the second *Hdac6*$^{-/-}$ iBMDM cell line, the following primers were used to verify the positive clones: forward primer: 5′-TGATTGTAGTCCAGAGTGAA-3′; reverse primer: 5′-AGCAGGTAGGATGAGACA-3′.

Transferrin-647 uptake assay

For uptake assays, WT and *Hdac6*$^{-/-}$ cells were grown on 35-mm dishes, serum starved for 30 min in DMEM with 0.5% BSA-containing medium, and incubated with 25 μg/ml Alexa Fluor 647–conjugated transferrin (Invitrogen, catalog no. T23366) at 4°C for 10 min. Unbound Alexa Fluor 647–conjugated transferrin was removed by brief washing. Transferrin uptake was then analyzed by confocal laser-scanning microscopy.

Knockdown of HDAC6 using siRNA and TRIM21 ubiquitin ligase in iBMDMs

For *Hdac6*-knockdown experiments using siRNA, iBMDMs were electroporated with two *Hdac6* Silencer siRNAs (Thermo Fisher Scientific, catalog nos. 67164 and 158920 for siRNAs #1 and #2, respectively) or with Silencer siRNA Negative Control (Thermo Fisher Scientific, catalog no. AM4611). For HDAC6 protein knockdown using TRIM21 ubiquitin ligase, iBMDMs (3.0×10^6) stably overexpressing mouse pSMPP-mCherry-TRIM21 (a gift from L. James, Addgene no. 104971) were electroporated either with 2 μg of rabbit anti-human HDAC6 IgG that cross-reacts with mouse HDAC6 (Cell Signaling Technology, catalog no. 7612) or with 2 μg of isotype control IgG (Agilent Dako, catalog no. X0903), respectively. Nucleofection of siRNAs and HDAC6 antibody was performed with the Nucleofector 2b device (Lonza, catalog no. AAB-1001) using the Y-001 program according to the manufacturer's recommendations. siRNA- and HDAC6 antibody–electroporated cells were incubated for 72 and 24 hours, respectively, before being processed for further experiments.

Flow cytometry–assisted Caspase-11 FLICA assay

For the Caspase-11 FLICA assay (ImmunoChemistry Technologies, catalog no. 97), after priming with LPS as described above, 1.0×10^6 buffer-electroporated and LPS-electroporated WT, *Nlrp3*$^{-/-}$, or *Nlrp3*$^{-/-}$/*Hdac6*$^{-/-}$ iBMDMs were incubated with medium containing 1× reconstituted fluorescently labeled inhibitor of active caspase (FAM-FLICA) and incubated for 1 hour. Cells were than washed three times with 1× apoptosis wash buffer and centrifuged at 218*g* for 10 min before being resuspended in regular DMEM and analyzed with a FACSAria II flow cytometer.

Mice

Male and female C57BL/6J WT and *Hdac6*$^{-/-}$ mice (8 to 10 weeks old) were purchased from The Jackson Laboratory (Bar Harbor, ME). Animals were housed in an animal facility for 3 days before any procedures. All animal experiments were performed in compliance with guidelines approved by the institutional animal care and use committee at the University of Michigan (protocol no. PRO00008861).

In vivo mouse model of endotoxic shock

Three experiments were performed. First, WT mice were randomly divided into three groups to test the effect of the HDAC6 inhibitor tubastatin A: (i) WT + dimethyl sulfoxide (DMSO) vehicle (1 μl/g mouse body weight), (ii) WT + lipopolysaccharides (LPS, 35 mg/kg in PBS; L2630; Sigma-Aldrich) + vehicle, and (iii) WT + LPS + tubastatin A (HDAC6 inhibitor, 70 mg/kg) + vehicle. Tubastatin A and vehicle were administered immediately after the intraperitoneal LPS challenge. Second, WT and *Hdac6*$^{-/-}$ mice were randomly divided into four groups to test the effect of *Hdac6* deletion: (i) WT + vehicle, (ii) WT + LPS + vehicle, (iii) *Hdac6*$^{-/-}$ + vehicle, and (iv) *Hdac6*$^{-/-}$ + LPS + vehicle. LPS and vehicle were similarly administered intraperitoneally. Third, WT mice were randomly divided into three groups to test the effect of the NLRP3 inhibitor MCC950: (i) WT + DMSO vehicle (1 μl/g mouse body weight), (ii) WT + LPS (35 mg/kg in PBS; L2630; SigmaAldrich) + vehicle, and (iii) WT + LPS + MCC950 (10 mg/kg) + vehicle. MCC950 and vehicle were administered 1 hour before the intraperitoneal LPS challenge. For all experiments, blood was collected at 12 hours after LPS injection. Serum was prepared by centrifugation of the blood at 500*g* at 4°C for 20 min and stored at −80°C for further use. Lung tissues were harvested for ALI scoring. Circulating levels of IL-1β and TNFα were measured using the mouse IL-1β/IL-1F2 DuoSet ELISA (DY401; R&D Systems) and mouse TNFα DuoSet ELISA (DY410-05; R&D Systems).

Histological analysis of ALI

Lung tissues were fixed in formalin and transferred to 70% ethanol before being embedded in paraffin and sliced into 5-μm sections. Hematoxylin & eosin staining was performed according to standard procedures. ALI scoring was performed by a pathologist blinded to the treatment assignment of the samples. In brief, ALI was classified into six categories based on the parameters of (i) septal mononuclear cell and/or lymphocyte infiltration, (ii) septal hemorrhage and congestion, (iii) neutrophils, (iv) alveolar macrophages, (v) alveolar hemorrhage, and (vi) alveolar edema. The severity of each category was graded from 0 (minimal) to 3 (maximal), and the total score was calculated by adding the scores in each of these categories.

In vivo mouse model of MSU-induced peritonitis

Peritonitis was induced by intraperitoneal injection of MSU crystals (1 mg; tlrl-msu-25; Invivogen) in 200 μl of sterile PBS with or without intraperitoneal pretreatment with MCC950 (10 mg/kg) at 25 hours and 1 hour before the MSU challenge. After 4 hours, mice were euthanized by CO_2 exposure. Peritoneal cavities were flushed with 5 ml of cold PBS. Peritoneal lavage was centrifuged at 94*g* for 5 min. Cell pellets were collected, and the recruitment of $CD45^+/Ly6G^+$ neutrophils into the peritoneal cavity was analyzed by flow cytometry. IL-1β levels were measured using ELISA (MLB00C; R&D Systems) after the peritoneal lavage supernatant was concentrated using an Amicon Ultra-0.5 Centrifugal Filter (UFC501096; Millipore).

Bone marrow isolation and BMDM differentiation

Bone marrow isolation and differentiation were performed in sterile and aseptic conditions in a laminar flow hood as described previously (*65*). The bones were flushed with 5 ml of PBS using a syringe fitted with a 25-G needle. The collected bone marrow was gently resuspended and passed through a 70-μm sterile cell strainer (Fisher Scientific, catalog no. 22363548). Cells were sedimented at 400*g* for 5 min at

Downloaded from http://science.sciencemag.org/ on September 18, 2020

room temperature. The cells were carefully collected in 100 × 20 mm sterile petri dishes containing 10 ml of conditioned media (DMEM + 10% FBS, penicillin/streptomycin, and 10% L929). On day 3, the dishes were supplemented with an additional 10 ml of conditioned medium (total 20 ml volume). Most cells were found to be adherent to the dish. Further growth was allowed until day 6, when the cells were split for the experiments performed on day 7.

FRET analysis

For FRET channel images, a 447-nm laser was used in conjunction with a 535/30 emission filter. All images were collected with a Yokogawa spinning-disk confocal on a Nikon Ti inverted microscope equipped with Plan Apo phase 3 oil-immersion 60× lens (1.4 NA). The Perfect Focus System was in place for continuous maintenance of focus. Image processing was mainly performed using MATLAB 2014b. Images were imported from the original files and sorted into channels. All metadata were extracted and saved. Dark current camera noise was corrected for using images acquired each session. Shading or "flat-field" correction based on empty fields from each sample was applied to correct for uneven illumination patterns. A background mask was generated by thresholding at a value three standard deviations above background, where the background intensity distribution is estimated by fitting the "left half" of a Gaussian function (the portion below its mean) to the left shoulder of the image intensity histogram. This mask was then used to find and subtract the average background intensity on a frame-by-frame basis. For all FRET calculations, the data were prefiltered with a 3 × 3 pixel Gaussian filter. Because the tension sensor module is a single-chain construct, FRET can be calculated by dividing the FRET channel fluorescence intensity (donor excitation with acceptor emission) with the mTurquoise2 channel fluorescence intensity (donor excitation with donor emission). To minimize artifacts from division of small integers, only pixels that had a value three times above the background standard deviation of the current frame were used. FRET data were visualized using an inverted heat map. The quantification of the loss of FRET inside and outside the puncta (as control) was performed using Fiji software on the inverted heat map.

Embedding in resin (plastic sections) for TEM

For transmission electron microscopy (TEM), iBMDMs after nigericin activation were processed for plastic embedding as follows. Cells were incubated in fixative for 1 hour at room temperature. A 2× fixative mixture was added in a 1:1 ratio to the medium in the dish containing the cells to prevent shock and allow gentle fixation. Fresh fixative was prepared using 1.25% paraformaldehyde, 2.5% glutaraldehyde, and 0.03% picric acid in a 0.1 M sodium cacodylate buffer, pH 7.4. After fixation, cells were washed three times in 0.1 M sodium cacodylate buffer, followed by incubation with 1% osmium tetroxide/1.5% potassium ferrocyanide for 1 hour at room temperature. Cells were then washed in water three times and incubated in aqueous 1% uranyl acetate for 30 min. This was followed by another three rounds of washing with water.

Dehydration steps were performed twice in grades of alcohol (70% ethanol for 15 min, 90% ethanol for 15 min, and 100% ethanol for 15 min. Samples were then placed in propyleneoxide for 1 hour and infiltration was performed with Epon mixed 1+1 with propyleneoxide for 2 to 3 hours at room temperature. Samples were moved to the embedding mold filled with freshly mixed Epon and allowed to polymerize for 24 to 48 hours at 60° C. Ultrathin sections (~60 nm) were cut on a Reichert Ultracut-S microtome, placed on copper grids, and stained with lead citrate. The grids from above-mentioned EM procedures were examined in a JEOL 1200EX 80 KeV TEM and images were recorded with an AMT 2k CCD camera (Harvard Medical School core facility).

Protein expression and purification

pET15b LFn-Fla and LFn-Fla 3A fusion constructs were transfected into *Escherichia coli* BL21 (DE3) cells and grown in LB medium supplemented with ampicillin. Cells were grown at 37°C until the optical density (600 nm) reached 0.8. Protein expression was induced with 0.2 mM isopropyl-β-D-thiogalactopyranoside at 18°C overnight. Cells were then harvested and resuspended in lysis buffer (20 mM Tris-HCl, pH 7.4, 150 mM NaCl, 10 mM imidazole, and 5 mM β-mercaptoethanol). The proteins were purified by affinity chromatography using Ni-NTA beads (Qiagen). The proteins were further purified to homogeneity by size-exclusion chromatography in lysis buffer (20 mM HEPES, pH 7.4, 150 mM NaCl, 2 mM dithiothreitol) on a Superdex-200 column (GE Healthcare Life Sciences). Protein purified to homogeneity was analyzed by SDS-PAGE.

REFERENCES AND NOTES

1. P. Broz, V. M. Dixit, Inflammasomes: Mechanism of assembly, regulation and signalling. *Nat. Rev. Immunol.* **16**, 407–420 (2016). doi: 10.1038/nri.2016.58; pmid: 27291964
2. V. A. Rathinam, S. K. Vanaja, K. A. Fitzgerald, Regulation of inflammasome signaling. *Nat. Immunol.* **13**, 333–342 (2012). doi: 10.1038/ni.2237; pmid: 22430786
3. M. Lamkanfi, V. M. Dixit, Mechanisms and functions of inflammasomes. *Cell* **157**, 1013–1022 (2014). doi: 10.1016/j.cell.2014.04.007; pmid: 24855941
4. T. Strowig, J. Henao-Mejia, E. Elinav, R. Flavell, Inflammasomes in health and disease. *Nature* **481**, 278–286 (2012). doi: 10.1038/nature10759; pmid: 22258606
5. M. Bäck, G. K. Hansson, Anti-inflammatory therapies for atherosclerosis. *Nat. Rev. Cardiol.* **12**, 199–211 (2015). doi: 10.1038/nrcardio.2015.5; pmid: 25666404
6. Q. Yin, T. M. Fu, J. Li, H. Wu, Structural biology of innate immunity. *Annu. Rev. Immunol.* **33**, 393–416 (2015). doi: 10.1146/annurev-immunol-032414-112258; pmid: 25622194
7. H. Xu *et al.*, Innate immune sensing of bacterial modifications of Rho GTPases by the Pyrin inflammasome. *Nature* **513**, 237–241 (2014). doi: 10.1038/nature13449; pmid: 24919149
8. F. Martinon, K. Burns, J. Tschopp, The inflammasome: A molecular platform triggering activation of inflammatory caspases and processing of proIL-beta. *Mol. Cell* **10**, 417–426 (2002). doi: 10.1016/S1097-2765(02)00599-3; pmid: 12191486
9. X. Liu *et al.*, Inflammasome-activated gasdermin D causes pyroptosis by forming membrane pores. *Nature* **535**, 153–158 (2016). doi: 10.1038/nature18629; pmid: 27383986
10. J. Ding *et al.*, Pore-forming activity and structural autoinhibition of the gasdermin family. *Nature* **535**, 111–116 (2016). doi: 10.1038/nature18590; pmid: 27281216
11. V. Hornung *et al.*, AIM2 recognizes cytosolic dsDNA and forms a caspase-1-activating inflammasome with ASC. *Nature* **458**, 514–518 (2009). doi: 10.1038/nature07725; pmid: 19158675
12. J. Wu, T. Fernandes-Alnemri, E. S. Alnemri, Involvement of the AIM2, NLRC4, and NLRP3 inflammasomes in caspase-1 activation by Listeria monocytogenes. *J. Clin. Immunol.* **30**, 693–702 (2010). doi: 10.1007/s10875-010-9425-2; pmid: 20490635
13. G. A. Pihan, Centrosome dysfunction contributes to chromosome instability, chromoanagenesis, and genome reprograming in cancer. *Front. Oncol.* **3**, 277 (2013). doi: 10.3389/fonc.2013.00277; pmid: 24282781
14. Y. He, M. Y. Zeng, D. Yang, B. Motro, G. Núñez, NEK7 is an essential mediator of NLRP3 activation downstream of potassium efflux. *Nature* **530**, 354–357 (2016). doi: 10.1038/nature16959; pmid: 26814970
15. H. Shi *et al.*, NLRP3 activation and mitosis are mutually exclusive events coordinated by NEK7, a new inflammasome component. *Nat. Immunol.* **17**, 250–258 (2016). doi: 10.1038/ni.3333; pmid: 26642356
16. J. L. Schmid-Burgk *et al.*, A Genome-wide CRISPR (clustered regularly interspaced short palindromic repeats) screen identifies NEK7 as an essential component of NLRP3 inflammasome activation. *J. Biol. Chem.* **291**, 103–109 (2016). doi: 10.1074/jbc.C115.700492; pmid: 26553871
17. E. Bedner, P. Smolewski, P. Amstad, Z. Darzynkiewicz, Activation of caspases measured in situ by binding of fluorochrome-labeled inhibitors of caspases (FLICA): Correlation with DNA fragmentation. *Exp. Cell Res.* **259**, 308–313 (2000). doi: 10.1006/excr.2000.4955; pmid: 10942603
18. F. Aguet *et al.*, Membrane dynamics of dividing cells imaged by lattice light-sheet microscopy. *Mol. Biol. Cell* **27**, 3418–3435 (2016). doi: 10.1091/mbc.e16-03-0164; pmid: 27535432
19. J. M. Hyttinen *et al.*, Clearance of misfolded and aggregated proteins by aggrephagy and implications for aggregation diseases. *Ageing Res. Rev.* **18**, 16–28 (2014). doi: 10.1016/j.arr.2014.07.002; pmid: 25062811
20. H. Ouyang *et al.*, Protein aggregates are recruited to aggresome by histone deacetylase 6 via unanchored ubiquitin C termini. *J. Biol. Chem.* **287**, 2317–2327 (2012). doi: 10.1074/jbc.M111.273730; pmid: 22069321
21. U. B. Pandey *et al.*, HDAC6 rescues neurodegeneration and provides an essential link between autophagy and the UPS. *Nature* **447**, 859–863 (2007). doi: 10.1038/nature05853; pmid: 17568747
22. Y. Kawaguchi *et al.*, The deacetylase HDAC6 regulates aggresome formation and cell viability in response to misfolded protein stress. *Cell* **115**, 727–738 (2003). doi: 10.1016/S0092-8674(03)00939-5; pmid: 14675537
23. R. R. Kopito, Aggresomes, inclusion bodies and protein aggregation. *Trends Cell Biol.* **10**, 524–530 (2000). doi: 10.1016/S0962-8924(00)01852-3; pmid: 11121744
24. T. Wileman, Aggresomes and pericentriolar sites of virus assembly: Cellular defense or viral design? *Annu. Rev. Microbiol.* **61**, 149–167 (2007). doi: 10.1146/annurev.micro.57.030502.090836; pmid: 17896875
25. I. Banerjee *et al.*, Influenza A virus uses the aggresome processing machinery for host cell entry. *Science* **346**, 473–477 (2014). doi: 10.1126/science.1257037; pmid: 25342804
26. A. Lu *et al.*, Unified polymerization mechanism for the assembly of ASC-dependent inflammasomes. *Cell* **156**, 1193–1206 (2014). doi: 10.1016/j.cell.2014.02.008; pmid: 24630722
27. B. H. Duong *et al.*, A20 restricts ubiquitination of pro-interleukin-1β protein complexes and suppresses NLRP3

Downloaded from http://science.sciencemag.org/ on September 18, 2020

inflammasome activity. *Immunity* **42**, 55–67 (2015). doi: 10.1016/j.immuni.2014.12.031; pmid: 25607459
28. M. A. Rodgers *et al*., The linear ubiquitin assembly complex (LUBAC) is essential for NLRP3 inflammasome activation. *J. Exp. Med.* **211**, 1333–1347 (2014). doi: 10.1084/jem.20132486; pmid: 24958845
29. K. Guan *et al*., MAVS promotes inflammasome activation by targeting ASC for K63-linked ubiquitination via the E3 ligase TRAF3. *J. Immunol.* **194**, 4880–4890 (2015). doi: 10.4049/jimmunol.1402851; pmid: 25847972
30. C. S. Shi *et al*., Activation of autophagy by inflammatory signals limits IL-1β production by targeting ubiquitinated inflammasomes for destruction. *Nat. Immunol.* **13**, 255–263 (2012). doi: 10.1038/ni.2215; pmid: 22286270
31. X. X. Wang, R. Z. Wan, Z. P. Liu, Recent advances in the discovery of potent and selective HDAC6 inhibitors. *Eur. J. Med. Chem.* **143**, 1406–1418 (2018). doi: 10.1016/j.ejmech.2017.10.040; pmid: 29133060
32. S. Florian, T. J. Mitchison, Anti-microtubule drugs. *Methods Mol. Biol.* **1413**, 403–421 (2016). doi: 10.1007/978-1-4939-3542-0_25; pmid: 27193863
33. A. J. Firestone *et al*., Small-molecule inhibitors of the AAA+ ATPase motor cytoplasmic dynein. *Nature* **484**, 125–129 (2012). doi: 10.1038/nature10936; pmid: 22425997
34. J. K. Burkhardt, C. J. Echeverri, T. Nilsson, R. B. Vallee, Overexpression of the dynamitin (p50) subunit of the dynactin complex disrupts dynein-dependent maintenance of membrane organelle distribution. *J. Cell Biol.* **139**, 469–484 (1997). doi: 10.1083/jcb.139.2.469; pmid: 9334349
35. T. Misawa *et al*., Microtubule-driven spatial arrangement of mitochondria promotes activation of the NLRP3 inflammasome. *Nat. Immunol.* **14**, 454–460 (2013). doi: 10.1038/ni.2550; pmid: 23502856
36. R. C. Coll *et al*., A small-molecule inhibitor of the NLRP3 inflammasome for the treatment of inflammatory diseases. *Nat. Med.* **21**, 248–255 (2015). doi: 10.1038/nm.3806; pmid: 25686105
37. Y. H. Park, G. Wood, D. L. Kastner, J. J. Chae, Pyrin inflammasome activation and RhoA signaling in the autoinflammatory diseases FMF and HIDS. *Nat. Immunol.* **17**, 914–921 (2016). doi: 10.1038/ni.3457; pmid: 27270401
38. H. Van Gorp *et al*., Familial Mediterranean fever mutations lift the obligatory requirement for microtubules in Pyrin inflammasome activation. *Proc. Natl. Acad. Sci. U.S.A.* **113**, 14384–14389 (2016). doi: 10.1073/pnas.1613156113; pmid: 27911804
39. P. D. Hsu, E. S. Lander, F. Zhang, Development and applications of CRISPR-Cas9 for genome engineering. *Cell* **157**, 1262–1278 (2014). doi: 10.1016/j.cell.2014.05.010; pmid: 24906146
40. D. Clift *et al*., A method for the acute and rapid degradation of endogenous proteins. *Cell* **171**, 1692–1706.e18 (2017). doi: 10.1016/j.cell.2017.10.033; pmid: 29153837
41. I. Hwang, E. Lee, S. A. Jeon, J. W. Yu, Histone deacetylase 6 negatively regulates NLRP3 inflammasome activation. *Biochem. Biophys. Res. Commun.* **467**, 973–978 (2015). doi: 10.1016/j.bbrc.2015.10.033; pmid: 26471297
42. Y. Miyake *et al*., Structural insights into HDAC6 tubulin deacetylation and its selective inhibition. *Nat. Chem. Biol.* **12**, 748–754 (2016). doi: 10.1038/nchembio.2140; pmid: 27454931
43. T. Hideshima *et al*., Small-molecule inhibition of proteasome and aggresome function induces synergistic antitumor activity in multiple myeloma. *Proc. Natl. Acad. Sci. U.S.A.* **102**, 8567–8572 (2005). doi: 10.1073/pnas.0503221102; pmid: 15937109
44. J. R. Cabrero *et al*., Lymphocyte chemotaxis is regulated by histone deacetylase 6, independently of its deacetylase activity. *Mol. Biol. Cell* **17**, 3435–3445 (2006). doi: 10.1091/mbc.e06-01-0008; pmid: 16738306
45. K. Nakahira *et al*., Autophagy proteins regulate innate immune responses by inhibiting the release of mitochondrial DNA mediated by the NALP3 inflammasome. *Nat. Immunol.* **12**, 222–230 (2011). doi: 10.1038/ni.1980; pmid: 21151103
46. T. Saitoh *et al*., Loss of the autophagy protein Atg16L1 enhances endotoxin-induced IL-1beta production. *Nature* **456**, 264–268 (2008). doi: 10.1038/nature07383; pmid: 18849965
47. K. W. Chen *et al*., Noncanonical inflammasome signaling elicits gasdermin D-dependent neutrophil extracellular traps. *Sci. Immunol.* **3**, eaar6676 (2018). doi: 10.1126/sciimmunol.aar6676; pmid: 30143554
48. S. Rühl, P. Broz, Caspase-11 activates a canonical NLRP3 inflammasome by promoting K(+) efflux. *Eur. J. Immunol.* **45**, 2927–2936 (2015). doi: 10.1002/eji.201545772; pmid: 26173909
49. S. M. Man *et al*., Inflammasome activation causes dual recruitment of NLRC4 and NLRP3 to the same macromolecular complex. *Proc. Natl. Acad. Sci. U.S.A.* **111**, 7403–7408 (2014). doi: 10.1073/pnas.1402911111; pmid: 24803432
50. N. Kayagaki *et al*., Non-canonical inflammasome activation targets caspase-11. *Nature* **479**, 117–121 (2011). doi: 10.1038/nature10558; pmid: 22002608
51. J. Shi *et al*., Inflammatory caspases are innate immune receptors for intracellular LPS. *Nature* **514**, 187–192 (2014). doi: 10.1038/nature13683; pmid: 25119034
52. J. von Moltke *et al*., Rapid induction of inflammatory lipid mediators by the inflammasome in vivo. *Nature* **490**, 107–111 (2012). doi: 10.1038/nature11351; pmid: 22902502
53. J. Chen, Z. J. Chen, PtdIns4P on dispersed trans-Golgi network mediates NLRP3 inflammasome activation. *Nature* **564**, 71–76 (2018). doi: 10.1038/s41586-018-0761-3; pmid: 30487600
54. H. Sharif *et al*., Structural mechanism for NEK7-licensed activation of NLRP3 inflammasome. *Nature* **570**, 338–343 (2019). doi: 10.1038/s41586-019-1295-z; pmid: 31189953
55. G. dos Santos *et al*., Vimentin regulates activation of the NLRP3 inflammasome. *Nat. Commun.* **6**, 6574 (2015). doi: 10.1038/ncomms7574; pmid: 25762200
56. Y. Liang *et al*., Inhibition of peptidylarginine deiminase alleviates LPS-induced pulmonary dysfunction and improves survival in a mouse model of lethal endotoxemia. *Eur. J. Pharmacol.* **833**, 432–440 (2018). doi: 10.1016/j.ejphar.2018.07.005; pmid: 29981294
57. X. Li *et al*., MARK4 regulates NLRP3 positioning and inflammasome activation through a microtubule-dependent mechanism. *Nat. Commun.* **8**, 15986 (2017). doi: 10.1038/ncomms15986; pmid: 28656979
58. M. Huse, A. Le Floc'h, X. Liu, From lipid second messengers to molecular motors: Microtubule-organizing center reorientation in T cells. *Immunol. Rev.* **256**, 95–106 (2013). doi: 10.1111/imr.12116; pmid: 24117815
59. M. Proell, M. Gerlic, P. D. Mace, J. C. Reed, S. J. Riedl, The CARD plays a critical role in ASC foci formation and inflammasome signalling. *Biochem. J.* **449**, 613–621 (2013). doi: 10.1042/BJ20121198; pmid: 23110696
60. D. Boucher *et al*., Caspase-1 self-cleavage is an intrinsic mechanism to terminate inflammasome activity. *J. Exp. Med.* **215**, 827–840 (2018). doi: 10.1084/jem.20172222; pmid: 29432122
61. J. C. Kagan, V. G. Magupalli, H. Wu, SMOCs: Location-specific higher-order signalling complexes that control innate immunity. *Nat. Rev. Immunol.* **14**, 821–826 (2014). doi: 10.1038/nri3757; pmid: 25359439
62. P. H. Ren *et al*., Cytoplasmic penetration and persistent infection of mammalian cells by polyglutamine aggregates. *Nat. Cell Biol.* **11**, 219–225 (2009). doi: 10.1038/ncb1830; pmid: 19151706
63. N. C. Shaner *et al*., Improving the photostability of bright monomeric orange and red fluorescent proteins. *Nat. Methods* **5**, 545–551 (2008). doi: 10.1038/nmeth.1209; pmid: 18454154
64. C. Jakobs, E. Bartok, A. Kubarenko, F. Bauernfeind, V. Hornung, Immunoblotting for active caspase-1. *Methods Mol. Biol.* **1040**, 103–115 (2013). doi: 10.1007/978-1-62703-523-1_9; pmid: 23852600
65. J. Weischenfeldt, B. Porse, Bone marrow-derived macrophages (BMM): Isolation and applications. *CSH Protoc.* **2008**, prot5080 (2008). doi: 10.1101/pdb.prot5080; pmid: 21356739
66. V. Neudecker *et al*., Neutrophil transfer of miR-223 to lung epithelial cells dampens acute lung injury in mice. *Sci. Transl. Med.* **9**, eaah5360 (2017). doi: 10.1126/scitranslmed.aah5360; pmid: 28931657
67. K. A. Shirey *et al*., The TLR4 antagonist Eritoran protects mice from lethal influenza infection. *Nature* **497**, 498–502 (2013). doi: 10.1038/nature12118; pmid: 23636320

ACKNOWLEDGMENTS

We thank J. Shah (Harvard Medical School), T. Mitchison (Harvard Medical School), and R. Vale (UCSF) for discussions; R. Mazitschek (Harvard Medical School) for discussions on HDAC inhibitors; G. Nuñez (University of Michigan) for *Nek7*$^{-/-}$ iBMDMs and for cDNA encoding human caspase-1; J. Yuan (Harvard Medical School) for cDNA encoding human IL-1β; M. Dong (Boston Children's Hospital) for recombinant full-length TcdB toxin; P. Matthias (Friedrich Miescher Institute for Biomedical Research) for human *HDAC6* and mouse *Hdac6* plasmids; Y. Zhang and J. Lieberman (Boston Children's Hospital) for anesthetizing and dissecting out the bones from mice; K. Rhee (Seoul National University) for NEK7 antibody; HCIA/HHMI summer institute, Woods Hole, and H. Leung (Optical Microscopy Core Facility of Program in Cellular and Molecular Medicine, Boston Children's Hospital) for help with laser scanning confocal microscopy; J. Waters and T. Lambert (Nikon Imaging Center, Harvard Medical School) for help with live-cell microscopy; R. Mathieu (Flow Cytometry Research Facility, Boston Children's Hospital) for help with cell sorting and cell analysis; and M. Ericsson (Electron Microscopy Core Facility, Harvard Medical School) for help with transmission electron microscopy.
Funding: This work was supported by the National Institutes of Health (grant nos. HD087988 and AI124491 to H.W., MIRA award no. GM130386 to T.K., and a T32 training fellowship to A.V.H.), Biogen (SRA to T.K.), and the Joint Institute of University of Michigan and Peking University Health Science Center (grant no. U068874 to Y.L.). T.K. acknowledges support from the Janelia Visitor Program and E. Betzig, E. Marino, T. Liu, G. Upadhyayula, and W. Legant for help and advice in constructing and installing the LLSM. Construction of the LLSM was supported by grants from Biogen and Ionis Pharmaceuticals to T.K. **Author contributions:** H.W. and V.G.M. conceived the project. V.G.M. and R.N. performed bulk assays, immunofluorescence, and live-cell imaging. V.G.M., R.N., and A.V.H. conducted molecular cloning and reconstitution. Y.T. and Q.D. performed in vivo experiments under Y.L.'s and H.B.A.'s supervision. G.D.C. and W.S. performed LLSM under T.K.'s supervision. P.O. helped with NLRC4 inflammasome assays and mouse primary cell experiments under K.A.F.'s supervision. F.I.S. provided the THP-1 cell line stably expressing ASC-tagRFP-T and certain NLRC4 activators. H.S. purified FlaTox. J.J.H. conducted caspase-11 FLICA assay. C.L.E. and J.C.K. helped with LPS electroporation. Z.M. provided discussions early in the project. H.W. supervised the project. H.W., V.G.M., and R.N. wrote the manuscript with comments from all authors. **Competing interests:** The authors declare no competing interests.
Data and materials availability: All data needed to evaluate the conclusions in this study are available in the main text and the supplementary materials.

SUPPLEMENTARY MATERIALS

science.sciencemag.org/content/369/6510/eaas8995/suppl/DC1
Figs. S1 to S20
Captions for Movies S1 to S20

View/request a protocol for this paper from *Bio-protocol*.

2 January 2018; resubmitted 7 July 2019
Accepted 13 July 2020
10.1126/science.aas8995

Downloaded from http://science.sciencemag.org/ on September 18, 2020

Science

HDAC6 mediates an aggresome-like mechanism for NLRP3 and pyrin inflammasome activation

Venkat Giri Magupalli, Roberto Negro, Yuzi Tian, Arthur V. Hauenstein, Giuseppe Di Caprio, Wesley Skillern, Qiufang Deng, Pontus Orning, Hasan B. Alam, Zoltan Maliga, Humayun Sharif, Jun Jacob Hu, Charles L. Evavold, Jonathan C. Kagan, Florian I. Schmidt, Katherine A. Fitzgerald, Tom Kirchhausen, Yongqing Li and Hao Wu

Science **369** (6510), eaas8995.
DOI: 10.1126/science.aas8995

The MTOC is "speck"-tacular

Inflammasome complexes are formed in response to pathogen-associated molecules. They initiate both the maturation of inflammatory cytokines and pyroptosis, a type of programmed cell death. One notable feature for inflammasome activation is the formation of a single supramolecular punctum (or "speck") in each affected cell. However, the location and mechanism of speck formation is poorly understood. Magupalli *et al.* report that for NLRP3- and pyrin-mediated inflammasomes, their assembly and downstream functions occur at the microtubule-organizing center (MTOC). This process requires the dynein adaptor HDAC6, which is also a central player in aggresome formation and autophagosomal degradation at the MTOC. This work links several important cellular processes and provides clues for how inflammasomes are efficiently regulated.

Science, this issue p. eaas8995

ARTICLE TOOLS http://science.sciencemag.org/content/369/6510/eaas8995

SUPPLEMENTARY MATERIALS http://science.sciencemag.org/content/suppl/2020/09/16/369.6510.eaas8995.DC1

RELATED CONTENT
http://stm.sciencemag.org/content/scitransmed/10/465/eaah4066.full
http://stm.sciencemag.org/content/scitransmed/8/358/358ra126.full
http://stm.sciencemag.org/content/scitransmed/8/332/332ra45.full
http://stm.sciencemag.org/content/scitransmed/10/456/eaam7510.full

REFERENCES This article cites 67 articles, 15 of which you can access for free
http://science.sciencemag.org/content/369/6510/eaas8995#BIBL

PERMISSIONS http://www.sciencemag.org/help/reprints-and-permissions

Use of this article is subject to the Terms of Service

Science (print ISSN 0036-8075; online ISSN 1095-9203) is published by the American Association for the Advancement of Science, 1200 New York Avenue NW, Washington, DC 20005. The title *Science* is a registered trademark of AAAS.

Copyright © 2020 The Authors, some rights reserved; exclusive licensee American Association for the Advancement of Science. No claim to original U.S. Government Works

Downloaded from http://science.sciencemag.org/ on September 18, 2020